

HIGH RESOLUTION MEASUREMENT OF LEVEE SUBSIDENCE RELATED TO ENERGY INFRASTRUCTURE IN THE SACRAMENTO-SAN JOAQUIN DELTA

A Report for:

California's Fourth Climate Change Assessment

Prepared By:

Benjamin A. Brooks¹, Jennifer Telling², Todd Ericksen¹, Craig L. Glennie², Noah Knowles³, Dan Cayan⁴, Darren Hauser², Adam LeWinter⁵

¹Earthquake Science Center

²National Center for Airborne Laser Mapping (NCALM)

³California Water Resources Center

⁴CASPO

⁵U.S. Army Corps of Engineers, Cold Regions Research and Engineering Laboratory

DISCLAIMER

This report was prepared as the result of work sponsored by the California Energy Commission. It does not necessarily represent the views of the Energy Commission, its employees or the State of California. The Energy Commission, the State of California, its employees, contractors and subcontractors make no warrant, express or implied, and assume no legal liability for the information in this report; nor does any party represent that the uses of this information will not infringe upon privately owned rights. This report has not been approved or disapproved by the California Energy Commission nor has the California Energy Commission passed upon the accuracy or adequacy of the information in this report.



Edmund G. Brown Jr., *Governor*

August 2018

CCCA4-CEC-2018-003

ACKNOWLEDGEMENTS

We thank Luke Blair and Fernando Martinez for their help with preliminary processing of the Airborne LIDAR data. Any use of trade, firm, or product names is for descriptive purposes only and does not imply endorsement by the U.S. Government. Support for this research was provided by the California Energy Commission Agreement Number 500-14-001.

PREFACE

California's Climate Change Assessments provide a scientific foundation for understanding climate-related vulnerability at the local scale and informing resilience actions. These assessments contribute to the advancement of science-based policies, plans, and programs to promote effective climate leadership in California. In 2006, California released its First Climate Change Assessment, which shed light on the impacts of climate change on specific sectors in California and was instrumental in supporting the passage of the landmark Assembly Bill 32 (Núñez, Chapter 488, Statutes of 2006), California's Global Warming Solutions Act. The Second Assessment concluded that adaptation is a crucial complement to reducing greenhouse gas emissions (2009), given that some changes to the climate are ongoing and inevitable, motivating and informing California's first Climate Adaptation Strategy released the same year. In 2012, California's Third Climate Change Assessment made substantial progress in projecting local impacts of climate change, investigating consequences to human and natural systems, and exploring barriers to adaptation.

Under the leadership of Governor Edmund G. Brown, Jr., a trio of state agencies jointly managed and supported California's Fourth Climate Change Assessment: California's Natural Resources Agency (CNRA), the Governor's Office of Planning and Research (OPR), and the California Energy Commission (Energy Commission). The Climate Action Team Research Working Group, through which more than 20 state agencies coordinate climate-related research, served as the Steering Committee, providing input for a multi-sector call for proposals, participating in selection of research teams, and offering technical guidance throughout the process.

California's Fourth Climate Change Assessment (Fourth Assessment) advances actionable science that serves the growing needs of state and local-level decision-makers from a variety of sectors. It includes research to develop rigorous, comprehensive climate change scenarios at a scale suitable for illuminating regional vulnerabilities and localized adaptation strategies in California; datasets and tools that improve integration of observed and projected knowledge about climate change into decision-making; and recommendations and information to directly inform vulnerability assessments and adaptation strategies for California's energy sector, water resources and management, oceans and coasts, forests, wildfires, agriculture, biodiversity and habitat, and public health.

The Fourth Assessment includes 44 technical reports to advance the scientific foundation for understanding climate-related risks and resilience options, nine regional reports plus an oceans and coast report to outline climate risks and adaptation options, reports on tribal and indigenous issues as well as climate justice, and a comprehensive statewide summary report. All research contributing to the Fourth Assessment was peer-reviewed to ensure scientific rigor and relevance to practitioners and stakeholders.

For the full suite of Fourth Assessment research products, please visit www.climateassessment.ca.gov. This report contributes to our understanding of energy sector resilience through acquisition of very high-resolution data portraying Delta subsidence in areas with natural gas infrastructure and analysis of how subsidence compounds risks related to sea level rise.

ABSTRACT

We assess flood overtopping potential (when flood water elevation exceeds levee elevation) to the levees surrounding the islands in the interior of California's Sacramento-San Joaquin Delta. Because critical natural gas infrastructure is susceptible to overtopping-related disruption, we focus our analysis on regions that are crossed by the network of the state's natural gas pipelines. We use laser scanning data collected during 2015-2016 to estimate subsidence rates since 2007 when an earlier, Delta-wide, airborne laser-scanning topographic dataset was collected. For each levee studied, we combine: (1) the estimated subsidence rate, (2) a conservative range of sea-level rise projections and, (3) an estimate of the 100-year freshwater flood stage to project the time until exceedance of the federal levee height standard (PL84-99). We find that subsidence rates vary from 0-5 centimeters per year (cm/yr) with mean values of ~1-2 cm/year. Local gradients in subsidence can be on the order of cms/yr over a distance of 10s of meters parallel to the levee crests, and these types of gradients are present near some pipeline crossings. The Sherman Island region has subsidence rates close to a factor of 2 greater than other areas considered. Our projections indicate general ranges of exceedance date from about 2060 (fast sea-level rise scenario) to 2080 (slow sea-level rise scenario) with some places projected to exceed threshold by about 2050.

Keywords: Sacramento-San Joaquin Delta, subsidence, levees, sea-level rise, LIDAR

Please use the following citation for this paper:

Brooks, Benjamin A., Jennifer Telling, Todd Ericksen, Craig L. Glennie, Noah Knowles, Dan Cayan, Darren Hauser, Adam LeWinter. (U.S. Geological Survey). 2018. *High Resolution Measurement of Levee Subsidence Related to Energy Infrastructure in the Sacramento-San Joaquin Delta*. California's Fourth Climate Change Assessment, California Energy Commission. Publication Number: CCCA4-CEC-2018-003.

HIGHLIGHTS

- Based on detailed measurements made in this study, subsidence rates for levees in the Sacramento-San Joaquin Delta can be on the order of centimeters per year (cms/yr).
- Delta levee subsidence is highly variable over fine spatial scales, with local gradients approaching values of cms/yr over 10s of meters parallel to the levee crests.
- Of particular pertinence to the natural gas infrastructure system, local subsidence gradients are present near some pipeline crossings.
- The portions of levees investigated in this research will fall under federal PL84-99 standards (1.5 feet freeboard above 100-year flood level) between 2050 and 2080 depending on sea-level rise and 100-year flood stage projections.

TABLE OF CONTENTS

ACKNOWLEDGEMENTS.....	i
PREFACE	ii
ABSTRACT	iv
HIGHLIGHTS.....	v
TABLE OF CONTENTS.....	vi
1: Introduction	1
1.1 Delta Natural Gas Pipeline Vulnerability to Sea-Level Rise.....	1
1.2 Sacramento Delta Subsidence	2
1.3 Levee Flood Design Standards & 100-year Flood Definition.....	4
1.4 Sea-Level Rise Projection	5
2: Data & Analysis	6
2.1 Airborne Laser Scanning (2007)	7
2.2 Airborne Laser Scanning (2015)	7
2.2.1 GNSS/IMU Data Processing.....	7
2.2.2 LIDAR Data Processing.....	7
2.3 Mobile Laser Scanning (2015-2016)	8
2.4 Vertical Land Motion Estimation.....	11
2.4.1 Filtering	11
2.4.2 Referencing	13
2.4.3 Preliminary Analysis	13
2.4.4 Levee Analysis.....	16
2.5 Water Level Projection: Sea-Level Rise and 100 Year Flood Stage Height	17
2.6 Overtopping Projection.....	20
3: Results	21
3.1 Gross VLM & Anthropogenic Signal	21
3.2 Subsidence.....	31

3.3 Overtopping Projections 39

3.4 Uncertainty 46

4: Discussion 47

5: Conclusions and Future Directions..... 48

6: References 49

APPENDIX A: VLM Rate Plots for Natural Gas Pipeline Crossings 1

1: Introduction

The purpose of this study is to make detailed measurements of subsidence (downward vertical land motion) associated with levees surrounding the islands in the Sacramento-San Joaquin Delta. The subsidence measurements can then be combined with sea-level rise projections and levee design thresholds to improve estimates of time-dependent, increasing susceptibility to levee flood overtopping. Our focus here is on overtopping because of its direct influence from rising sea-level trends; however, it is only one of a multitude of potential levee failure modes including foundation scouring, seepage, and foundation deformation (Ojha, Singh et al. 2001, Serre, Peyras et al. 2008, Sills, Vroman et al. 2008, Huang, Weng et al. 2014). Furthermore, because of its importance to the State of California's daily functioning, our study focuses on where energy infrastructure, specifically gas pipelines, intersect the Delta's levees.

1.1 Delta Natural Gas Pipeline Vulnerability to Sea-Level Rise

The state of California's population and economy is critically reliant upon natural gas. In 2016, for instance, natural gas accounted for ~50% of total system electric generation (http://www.energy.ca.gov/almanac/electricity_data/total_system_power.html). For comparison, hydro-power was the next-most relied upon source and accounted for ~12% of electrical system generation. Accordingly, ensuring the integrity of the California-wide intrastate natural gas transmission, gathering, and distribution system is of vital importance to the general well-being of the state, especially given the increasing recognition of the effects of climate change (Kennedy, Bauer et al. 2014). Of particular concern is the fact that California's natural gas infrastructure was designed and built in the previous century when climate-change effects were not as well understood nor considered (Radke, Biging et al. 2016).

The Sacramento Delta is a focal point for natural gas in the State. It hosts a network of natural gas supply pipelines to many points in the State and, in particular, to the urban population hub of the San Francisco Bay Area (Radke, Biging et al. 2016) (Fig. 1). As with all critical infrastructure along California's waterways, the pipeline system is vulnerable to adverse inundation effects exacerbated by sea level rise (SLR) (Heberger, Cooley et al. 2009). The Delta's Economic Sustainability Plan states: "A large portion of the Delta's natural gas infrastructure is located within the Delta's 100-year floodplain and as such may be damaged and disrupted during flooding events." Inundation effects on pipeline infrastructure include: increased hydrostatic load; erosion, scouring and debris flows; corrosion; and restriction of access (Radke, Biging et al. 2016). Given that SLR rate is projected to accelerate throughout the 21st century (Board 2012), the higher frequency, duration, and/or depth of inundation from future flooding could exceed pipeline design standards as seen in other recent high-water events (Needham, Brown et al. 2012).

Local Vertical Land Motion (VLM), if it is downward (commonly termed 'subsidence'), can amplify relative sea-level rise by a factor of two or more (Brooks, Merrifield et al. 2007). We refer the reader to Radke, Biging et al. (2016) for detailed explication of pipeline structures,

engineering, and vulnerability, but it is clear that assessing VLM close to pipelines is necessary to better understand and plan for how the Delta's natural gas pipeline network will be affected by future SLR.

1.2 Sacramento Delta Subsidence

Land subsidence in the Delta has been occurring since the late 1800s and it has left island elevations as much as ~8m below sea level (Mount and Twiss 2005, Coons, Soulard et al. 2008) (Fig. 1). Generally, the subsidence has been considered the result of microbial oxidation, compaction, and wind-erosion of near-surface peat soils drained for agricultural purposes (Rojstaczer, Hamon et al. 1991, Rojstaczer and Deverel 1993, Rojstaczer and Deverel 1995, Deverel and Rojstaczer 1996, Deverel, Wang et al. 1998, Mount and Twiss 2005, Deverel and Leighton 2010). This process has been measured at rates of centimeters per year (Rojstaczer, Hamon et al. 1991, Rojstaczer and Deverel 1993, Rojstaczer and Deverel 1995, Deverel and Rojstaczer 1996, Deverel, Wang et al. 1998, Mount and Twiss 2005, Deverel and Leighton 2010) and the rate in some locations has slowed since the 1950s due to implementation of improved land use technique (Deverel and Rojstaczer 1996, Deverel, Wang et al. 1998, Mount and Twiss 2005).

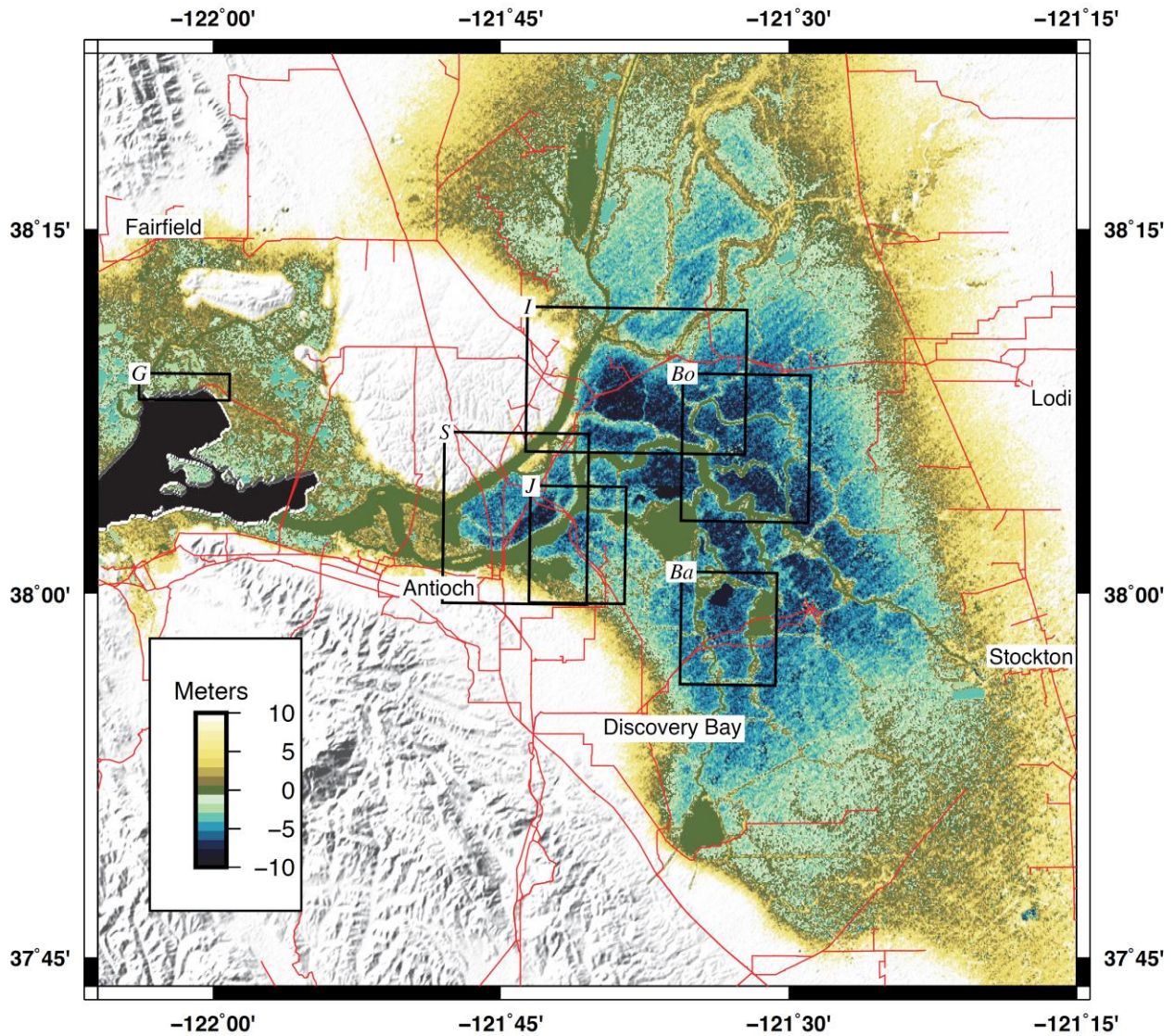


Figure 1. Location map of the Sacramento-San Joaquin Delta. Topographic base map, SRTM 90 meter elevation dataset. Red lines, natural gas pipeline network. Black rectangles, specific study areas: G, Grizzly Island; I, Isleton Island; S, Sherman Island; Bo, Bouldin Island; J, Jersey Island; Ba, Bacon Island.

Delta subsidence rates, typically on the order of centimeters per year, have been measured most typically by traditional surveying methods (Deverel and Rojstaczer 1996, Deverel, Wang et al. 1998, Deverel and Leighton 2010). To study subsidence more regionally, Mount and Twiss (2005) used Delta-wide topographic data (Shuttle Radar Topographic Mission, SRTM, 30m posting) to measure land changes since the start of the 20th century. We showed that satellite-based InSAR (interferometric synthetic aperture radar) provides unprecedented ability to synoptically monitor Delta-wide subsidence rates over periods of months to years. Due to decorrelation of C-band radar, however, particularly over vegetated areas, the technique is

more applicable to hard levee crests rather than island interiors (Brooks, Bawden et al. 2012, Brooks and Majunath 2012). These measurements illuminated levee-specific average rates of 1-3mm/yr that we interpreted to reflect the ongoing compaction of the Quaternary sedimentary section across the entire Delta (Brooks, Bawden et al. 2012, Brooks and Majunath 2012). More recently, L-band, airplane-based SAR (Unmanned Aerial Vehicle Synthetic Aperture Radar, UAVSAR) with monthly repeat passes has been shown to not be as sensitive to decorrelation, permitting island interior subsidence rates from ~1-5cm/yr at Sherman Island 2009-2014 to be determined (Sharma, Jones et al. 2016).

Because the measured subsidence rates in the Delta can be up to 70 times the currently observed rate of global Sea Level Rise (~1–3 mm/yr) (Church and White 2006, Woppelmann, Letetrel et al. 2009), quantifying Delta-wide subsidence is essential to best inform planning and mitigation decisions. Because most of the Delta islands lie significantly below sea-level, breaches in protective levees are significant threats to energy infrastructure. Accordingly, decrease in levee and island interior elevations through subsidence, especially in the context of increasing sea-level scenarios, exacerbates the threats by making the levees more susceptible to a variety of failure modes. For instance, the motion of the crest is critical in assessing water-level hazards such as scouring or overtopping when flood water elevation exceeds levee elevation (Tung and Mays 1981). In contrast, island interior subsidence affects mechanical factors (hydraulic head changes) that ultimately drive the deformation and distortion of the trapezoidal levee shape.

Recently, the proliferation of high-resolution LIDAR (Light Detection and Ranging) topographic data sets presents the possibility of making VLM estimates over greater spatial regions than traditional surveying techniques and over longer time-scales than SAR techniques. This is because LIDAR VLM analysis from differencing of digital elevation models does not require coherence of the ground between observational epochs. In general, vegetation, through which infrared-wavelength laser pulses have difficulty penetrating, is a confounding factor for most types of LIDAR analysis and there is a large sub-field based around devising vegetation-removal algorithms (Wang and Glenn 2009). Compact and portable Mobile Laser Scanning (MLS) platforms (Brooks, Glennie et al. 2013) are especially well-suited for the pertinent spatial and temporal scales. We showed that a balloon-based MLS system when referenced to the Delta-wide airborne LIDAR data set (Dudas 2009) determined subsidence of Sherman island levees at rates of cms/yr (Glennie, Brooks et al. 2013). Similarly, ground-based LIDAR was used to determine cms of subsidence over tens of meters length during a focused seepage experiment on Twitchell island (Bawden, Howle et al. 2014).

1.3 Levee Flood Design Standards & 100-year Flood Definition

Design standards in the Delta are variable though two are typically used (Suddeth, Mount et al. 2010). The HMP (Hazard Mitigation Plan) was defined by the State of California as 1 foot freeboard above the 100 year flood. PL84-99 is 1.5 foot freeboard above a 100 year flood elevation and is a federal standard (Suddeth, Mount et al. 2010) (Fig. 2). PL 84-99 is the target standard for two-thirds of Delta levees although few meet this criteria; more conform to HMP

(Suddeth, Mount et al. 2010). The definition of the 100 year flood is model dependent (Department of the Army 1976, Department of the Army 1982, Department of the Army 1992). For this study, despite the existence of more recently conducted studies, we choose the 1976 Army Corps of Engineers study for 100 year flood heights based on its wide utilization throughout the Delta (Department of the Army 1976).

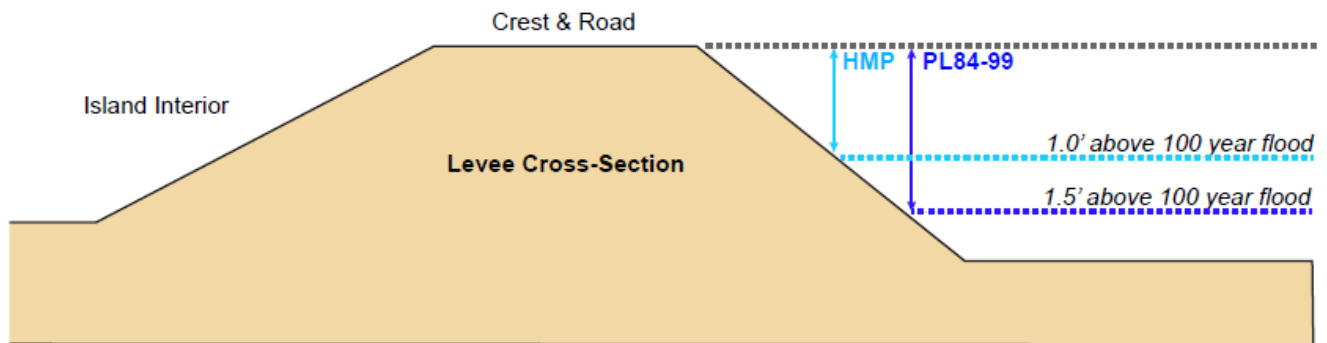


Figure 2. Levee design standards (after Suddeth et al., 2010). PL84-99 is a Federal standard and HMP (Hazard Mitigation Plan) was defined by the State of California. This study uses the PL84-99 standard.

1.4 Sea-Level Rise Projection

Generally, global Sea Level Rise (SLR) projections comprise contributions from five principal components: ocean thermal expansion, glacier melt, ice sheet melting in Antarctica and Greenland, and surface water sequestration (Cayan, Kalansky et al. 2016). Uncertainty in the projections results from variable knowledge of the physics of the processes and capability to monitor and model the contributions. Currently, the State of California uses the National Research Council (NRC) Report (Board 2012) as the guideline for SLR-related planning. The report includes a range of 21st century SLR projections guided by expert opinion. In the years since the NRC report was published, however, new studies have refined the possible contribution of important SLR components, in particular, the West Antarctic Ice Sheet (WAIS) (DeConto and Pollard 2016). These studies strongly suggest that previous SLR projections were probably too low.

For this report, we employ the recent projections developed for the 4th California Climate Assessment (Cayan, Kalansky et al. 2016). Similar projections were also employed for the updated California Sea-Level rise guidance report (Griggs, Árvai et al. 2017). These probabilistic projections follow existing methodology (Kopp, Horton et al. 2014) modified by the recent results for the additional West Antarctic Ice Sheet contribution (DeConto and Pollard 2016). The Kopp et al. (2014) method creates a time-dependent probability distribution of the different components, assumed independent of one another, and samples them to calculate SLR

probabilities. We refer the reader to Cayan, Kalansky et al. 2016, Kopp, Horton et al. 2014 and (Griggs, Árvai et al. 2017) for thorough descriptions of the methodologies.

2: Data & Analysis

For this study we used 3 different types of LIDAR data: (1) Airborne Laser Scanning (ALS) collected in 2007 for the California Department of Water Resources; (2) ALS collected by our team for this study in 2015; and (3) Mobile Laser Scanning (MLS) by our team for this study in 2015/2016. Table 1 summarizes the collection instruments and below we discuss each dataset's acquisition parameters. The 2007 ALS dataset is what we use as the reference dataset for all VLM estimates (see below).

Table 1. Metrics describing the 3 LIDAR datasets used by this study. The ALS 2015 and all MLS data were collected as part of this study.

	ALS 2007 (late Jan/Feb)	ALS 2015	MLS 2015/16
Height (m)	1700	800	2.75
Speed (m/s)	62	46.3	2-5
Pulse Rate (kHz)	70	300	300
Beam Divergence (mRad)	0.3	0.3	0.3
Scan Frequency (Hz)	50	62	120
Field of View (deg)	±24	±30	100 (+60/-40)
Flightline Overlap (%)	40	50	N/A
Point Density (pts/m ²)	0.8	10	800
agency	DWR	NCALM/USGS/CRREL <i>(this study)</i>	USGS <i>(this study)</i>

2.1 Airborne Laser Scanning (2007)

The first dataset was collected in late January and February of 2007 by URS Corporation/ Fugro EarthData, under contract by the California Department of Water Resources (Dudas 2009). The final 2007 data product was classified by NOAA into 3 data classes: ground (including bare earth and water returns), noise, and 'unclassified'; the only reference to the data set and its processing is found online (https://coast.noaa.gov/htdata/lidar1_z/geoid12a/data/2523/).

2.2 Airborne Laser Scanning (2015)

In August 2015 repeat ALS data was collected by the National Center for Airborne Laser Mapping (NCALM) and the Cold Regions Research and Engineering Laboratory (CRREL) and processed by NCALM. The data were acquired on August 20, 2015 by NCALM and the Cold Regions Research and Engineering Laboratory using a Riegl Q-680i sensor flown in a Partenavia P68.

2.2.1 GNSS/IMU Data Processing

Reference coordinates (customarily NAD83(2011) epoch 2010.00) for all stations are derived from observation sessions taken over the project duration and submitted to the National Geodetic Survey's (NGS) on-line processor OPUS, which processes static differential baselines tied to the international CORS network. For further information on OPUS see: www.ngs.noaa.gov/OPUS, and for more information on the CORS network see: www.ngs.noaa.gov/CORS.

Aircraft trajectories are processed using Kintools software, written by Dr. Gerald L. Mader of the NGS Research Laboratory. Kintools kinematic GPS processing uses the dual-frequency phase history files of the reference and airborne receivers to determine a high-accuracy, fixed integer, ionosphere-free differential solution at 1 Hz. All final aircraft trajectories for projects (except in rare instances) are blended solutions from at least two of the available reference stations. For more information on Kintools, see: www.generalpositioning.com.

After GPS processing, the 1-Hz trajectory solution and the 200-Hz raw inertial measurement unit (IMU) data collected during the flights are combined in APPLANIX software POSPac MMS (currently Mobile Mapping Suite Version 7.1 SP2). POSPac MMS implements a Kalman filter algorithm to produce a final, smoothed, and complete navigation solution, including both aircraft position and orientation at 200 Hz. This final navigation solution is known as an SBET (Smoothed Best Estimated Trajectory).

2.2.2 LIDAR Data Processing

NCALM is a NSF facility for the collection of airborne laser scanning data for the scientific community. It has been collecting, processing, and delivering ALS data for over a decade (Glennie, Carter et al. 2013). For description of the general NCALM products we refer the reader to Glennie, Carter et al. 2013, and we summarize in Fig. 3 a general overview of the NCALM LIDAR data processing workflow.

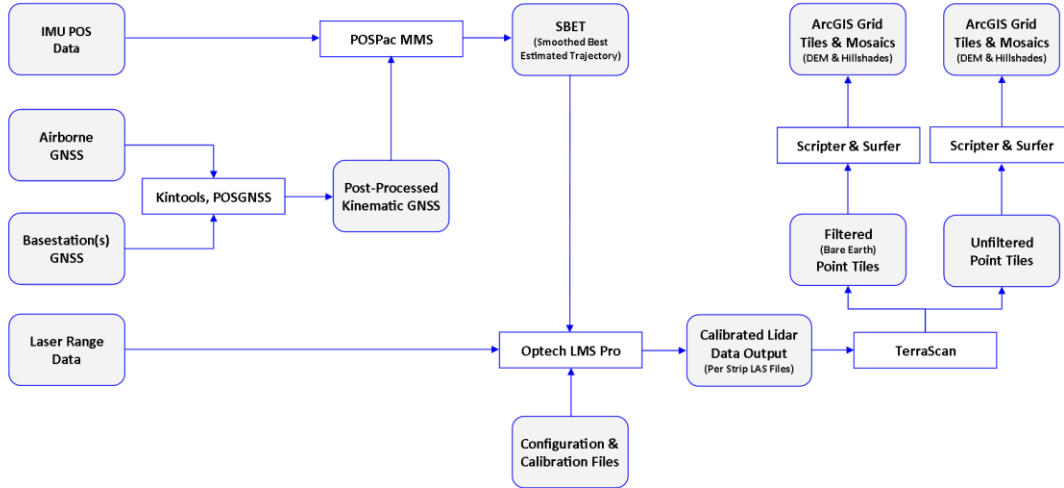


Figure 3. Flowchart depicting the NCALM (National Center for Airborne Laser Mapping) ALS (airborne laser mapping) standard processing strategy.

2.3 Mobile Laser Scanning (2015-2016)

Our Mobile Laser Scanning platform sits on an elevated rack at the back of the bed of a Dodge 2500 4x4 pickup (Fig. 4). The system comprises two laser scanners mounted on a machined plate along with an inertial navigation system (INS) and dual-frequency GPS receiver/antenna pair (Fig 4). Elsewhere we have described our general MLS processing approach resulting in a georeferenced point cloud with a WGS84 datum (Glennie, Brooks et al. 2013). In Table 2 and below we give specifics of the MLS acquisition and processing for this project.

Table 2. MLS acquisition locations and dates.

Location	Date
Jersey	20 July, 2015
Bacon	3 February, 2016
Bouldin	23 February, 2016
Isleton	15 September, 2016



Figure 4. Photos showing; A) the MLS (mobile laser scanning) truck operated by the USGS and employed for this study and B) the equipment rack showing dual laser scanners, IMU (inertial motion unit), and GNSS antenna.

We acquire MLS data with two Riegl VZ laser scanners: a VZ400 on the port/left/driver side of the vehicle, and a VZ1000 on the starboard/right/passenger side of the vehicle. The scanners log data during the survey directly to a field laptop in the vehicle. We simultaneously acquire high precision position and orientation data using an IxBlue ATLANS-C INS. The ATLANS-C stores high rate (200Hz) data from 3 accelerometers and 3 fiber optic gyroscopes and an integrated multi-frequency Septentrio GNSS receiver. These data are logged locally on the ATLANS-C throughout the survey. At the conclusion of a survey we download the data from the ATLANS-C to the field laptop and an external USB hard drive. Upon return from the field we copy the survey data to a RAID Level 5 data archive.

Kinematic processing of the ATLANS-C rover GNSS data requires additional base station GNSS data from at least one continuously operating reference station recording data at 1Hz or better within 10km of the survey area. For this study, we used 1Hz data archived by UNAVCO (www.unavco.org/instrumentation/networks/status/pbo) or the Northern California Earthquake Data Center (NCEDC, <http://ncedc.org/>). For some surveys we also operated our own TopCon G3A GNSS receiver as a base station for surveys when a nearby 1Hz base station was not available.

UNAVCO and NCEDC archive RINEX data which does not include GNSS navigation information. We download broadcast ephemeris data containing all broadcast ephemeris messages required for post-processing from CDDIS (cddis.nasa.gov). For our own TopCon G3A receiver the ephemeris data are recorded in the binary file and we generate the navigation data file during the translation to RINEX. We use 'Teqc' software available from UNAVCO to translate the TopCon binary data to RINEX format. We then check all base station RINEX data for completeness and quality during the survey time window using teqc. For each base station, we create a windowed RINEX file encompassing the survey with an additional 30-60 minutes of static data included at the beginning and end of the survey. We then compute the precise position of each base station by uploading each file and station antenna and radome configuration to NOAA's Online Positioning User Service (OPUS, www.ngs.noaa.gov/OPUS/).

We combine the base station GNSS files and associated navigation data and convert them from RINEX to Septentrio binary format for use in processing the final trajectory. During conversion using IxBlue 'rin2sbf' software, we compute the Doppler shift from the carrier phase and ignore the Dx observable.

We compute the trajectory using the ATLANS Post Processing Suite (APPS) software provided by IxBlue. APPS must initially convert the raw LOG format from the ATLANS-C into an xpf format for processing. We then check the solution for quality and the processing parameters and refine as needed. We perform an initial check of the trajectory with an elevation mask of 10 degrees. We import base station data with manually defined positions from the OPUS solution. We select the 'rough alignment' of the ATLANS relative to vehicle reference frame and input the lever arm offset of the GNSS rover antenna reference point to the ATLANS-C center of measurement. We set the output rate to 0.1s and solve for the trajectory. The solution consists of a number of variables recorded as an extensible markup language (xml) file. We review the standard deviations (sd) of the results in APPS, examining in particular the values of Navigation at Primary northing sd, easting sd, GNSS northing sd and easting sd, Navigation at Primary, roll sd, pitch sd, and heading sd. If the results are acceptable, we re-run the solution with an output rate of 0.005s. We re-check the standard deviations of the results and ensure that final navigation standard deviations of less than 0.015m were achieved.

We then convert the Reigl binary LIDAR data and calibrate the laser scanner boresight angles. The boresight calibration must be done every time the system is set up in order to accurately align the position and orientation of the Reigl VZ reference frame with the ATLANS-C reference frame. We perform conversion and calibration using two programs specifically written for the USGS MLS system (Glennie, Brooks et al. 2013).

We use the program 'rxp_georeference.exe' to convert proprietary Riegl .rxp files to open standard LAS (LASer Exchange Format) files. 'Rxp_georeference' is run in either "Production" or "Calibration" mode: Calibration mode generates LAS files with a unique shot number stored in place of GPS time and a single binary file for use by the calibration program. Production mode generates LAS files with correct GPS times. We run Production mode after obtaining the calibrated boresight angles to generate final, calibrated LIDAR point clouds (three-dimensional points representing each LIDAR reflection).

We use the program 'calibration.exe' to compute corrected boresight angles from planar extractions of data from the survey. We convert LIDAR data for calibration from Riegl binary format to LAS format using rxp-georeference.exe, in calibration mode, with a configuration file containing rough alignment data. This generates both a file containing calibration data and LAS files output with unique shot number in place of GPS time. We import the LAS files into the software package Terrascan with data from each scanner imported on separate flight lines. We identify planar areas within each point cloud that contain multiple passes of each laser from different distances and angles of approach. We select points from these planar areas and classify them as distinct planes. We classify a total of 30-50 and exported them as a separate LAS file.

We then input the LAS file of planes, the calibration data file, trajectory, and other configuration parameters, into the calibration.exe program which calculates a best fit boresight for alignment of the points within each plane. The result is a corrected roll, pitch, and heading offset for the laser scanners, and an error estimation of the fit. We then use these corrected boresight angles to create a final configuration file for rxp-georeference.exe. We run rxp-georeference one final time in “production mode” to output the final geo-referenced (WGS84 datum) point cloud.

2.4 Vertical Land Motion Estimation

Our objective is to calculate Vertical Land Motion (VLM) in a three-dimensional coordinate system aligned with a Universal Transverse Mercator projection (zone 10) with East, North, and Up axes (\hat{e} , \hat{n} , \hat{u}). VLM is the difference in the \hat{u} direction of two LIDAR elevation data sets ($VLM = D_2 - D_1$; where the $D_i(e,n)$ represent different acquisition epochs, i . In all of our analyses, D_1 is the 2007 ALS dataset, so $VLM > 0$ reflects elevation increase with time and $VLM < 0$ reflects subsidence, or elevation decrease with time. As described below, before we calculate VLM we undertake a number of preparatory steps for the data sets.

2.4.1 Filtering

The ALS and MLS datasets were both filtered to remove LIDAR returns and features outside the feature of interest, such as buildings, trees, and powerlines, that might lead to an incorrect determination of the levee road position (Fig. 5). While both the ALS and MLS data required filtering, the MLS data required far more filtering since MLS point density is significantly higher than that in the ALS data.

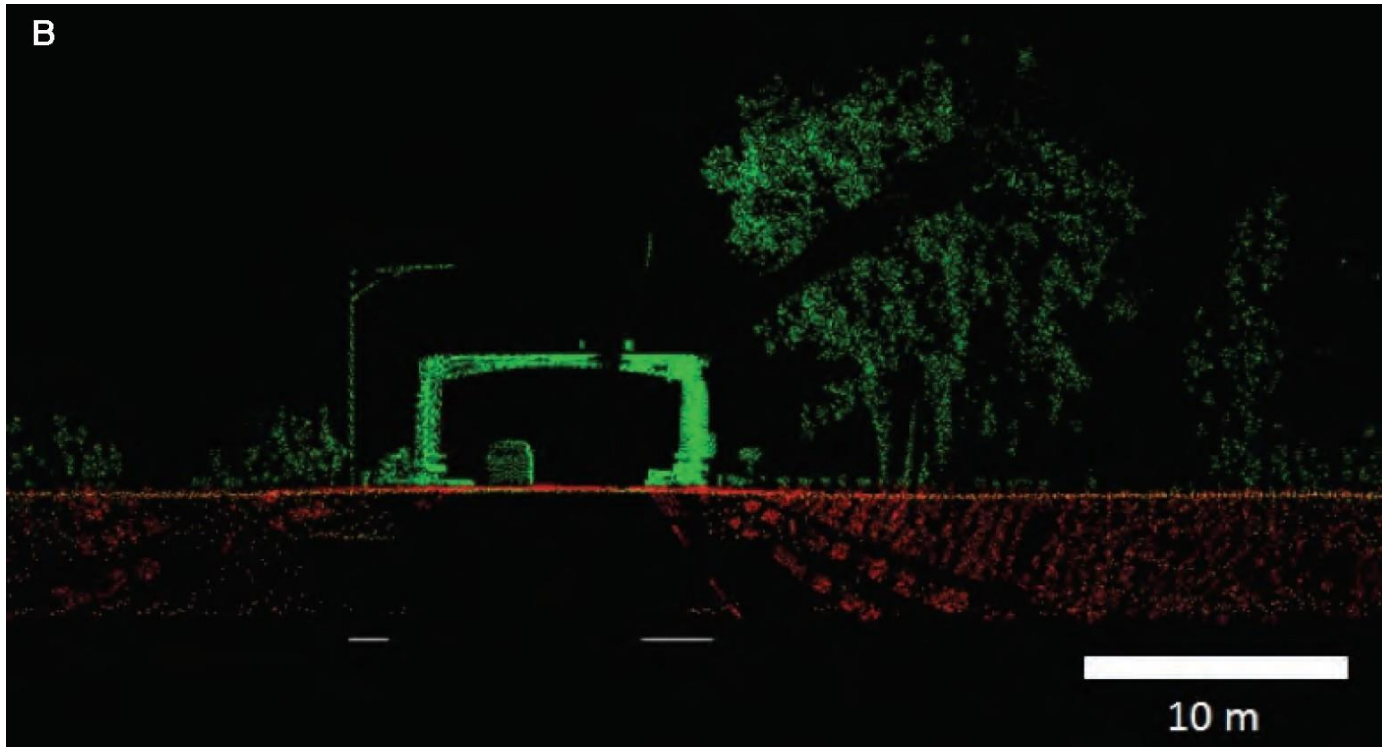
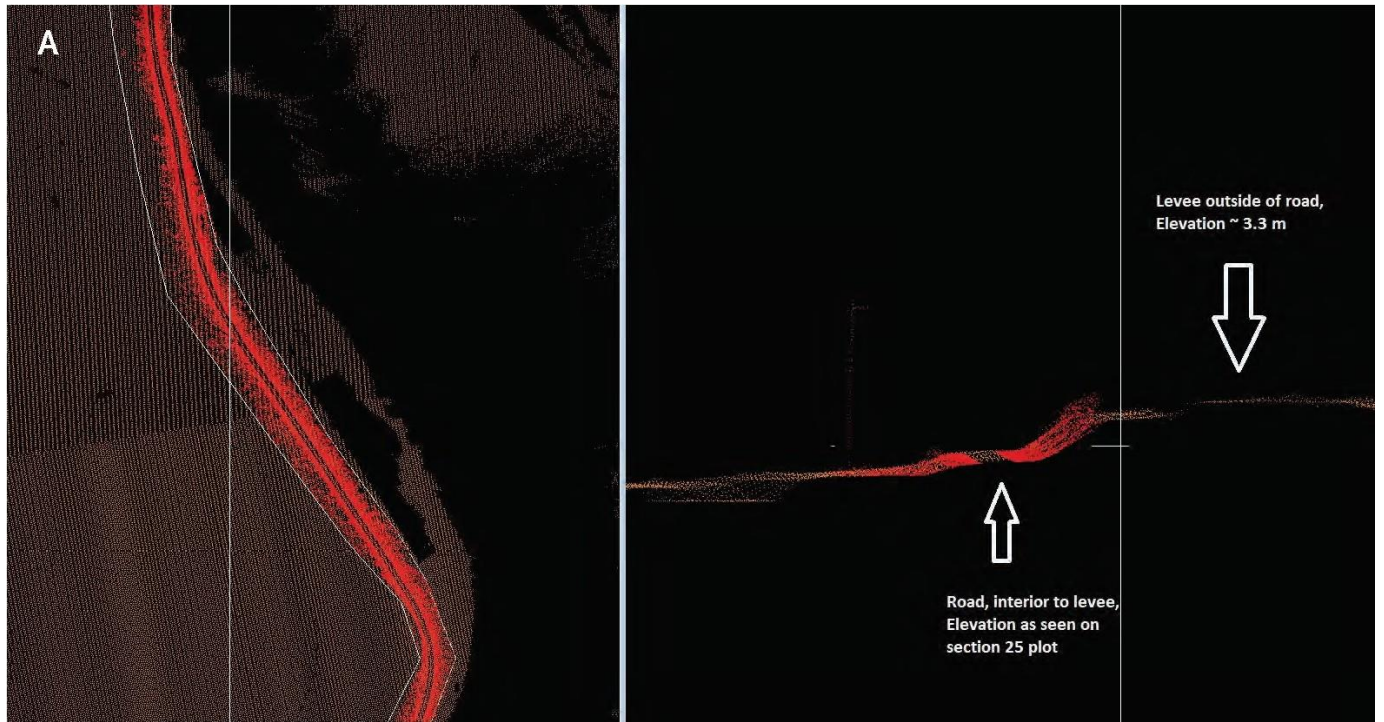


Figure 5. A) Example point cloud (map view) and cross-section from a segment of a levee road showing typical scanning coverage and definition of the levee road. All data from the left panel are collapsed into the right panel cross-section. B) Cross-sectional example of a point cloud with nuisance features (trees, lamp-posts, built structures, cars) that are removed by manual filtering.

2.4.2 Referencing

In order to difference D_1 with subsequently collected data sets (D_2 , either MLS or ALS) the two data sets must be first referenced to one another. Specifically, we: a) place the data sets in the same geographic coordinate system (including vertical datum) and b) remove any horizontal displacements caused by global plate tectonic motion (Pearson and Snay 2013). Because our dataset referencing approach only considers horizontal adjustments, any vertical motions caused by local or regional vertical tectonics is not accounted for. We believe that these vertical adjustments are likely negligible. For instance, there is no evidence of local tectonic activity at levels significant enough to cause measurable vertical motion (Brooks and Majunath 2012). Additionally, the signal of glacial isostatic adjustment (GIA) in the Delta is highly model dependent and untested; at most it would account for $\sim 1\text{-}2\text{mm/yr}$ of subsidence (Brooks and Majunath 2012).

The 2007 ALS data were received with the horizontal datum in NAD83 and the vertical datum in NAVD88, realized using the Geoid12A model from NGS. The 2015 ALS and 2015/2016 MLS point clouds were processed using the same horizontal and vertical datum (including geoid model). Primary base station locations were determined in NAD83 using the NGS Online Positioning Users Service (OPUS). Ellipsoidal heights for all point clouds were then transformed to NAVD88 using the Geoid12A model from the NGS. The positions of man-made structures, including buildings, bridges, and roads, were used to verify that the datasets were properly aligned. We transformed all data into WGS84 using NGS's online Horizontal Time Dependent Positioning software (<https://www.ngs.noaa.gov/TOOLS>) that also removes the plate-tectonic related horizontal displacements from D_2 . This datum transformation is a simple x,y,z shift. Given the relatively small spatial scale of the delta surveys, any error due to the transformation is at least an order of magnitude less than the expected signals.

2.4.3 Preliminary Analysis

We performed a preliminary analysis on the datasets in order to develop, test, and refine our analysis strategy. In the first example, we present the raw VLM calculation where D_2 is the 2015 ALS dataset over Grizzly Island (Fig. 6). It is immediately apparent that there are large, positive VLM artifacts in the northeastern portion of the VLM map. These express themselves as a general positive bias that is distinctly aligned with a wnw-trending positive VLM discontinuity. We identified that this discontinuity — as well as the second, nnw-trending discontinuity — are flightline mismatches that are contained within the 2007 ALS dataset (Fig. 7). Because we do not have access to the raw 2007 ALS data we have no way of correcting these processing artifacts, and so the vertical shift associated with them would contaminate any analysis such as differencing with the 2015 ALS data set.

There are also large apparent positive VLM signals associated with all of the inter-island river tributaries (Fig. 6). These and other positive VLM patches distributed throughout the island interiors are all associated with vegetation growth between 2007 and 2015. By comparing one of

our MLS datasets with the 2007 ALS dataset, we clearly identify that some type of vegetation filtering ('bare-earthing') was applied to the 2007 data (Fig. 8). Because a description of this filtering is not available in the documentation for the 2007 ALS dataset, this would represent a major uncertainty in any kind of VLM analysis over vegetated areas. Accordingly, where the preliminary 2015-2007 ALS identifies negative VLM values in the island interiors (Fig. 6), it is impossible for us to unambiguously separate actual VLM from either an effect caused by the bare-earthing of the 2007 dataset or any vegetation loss (such as mowing or crop harvesting) in the 2007-2015 time period.

The combination of the presence of vegetation changes with 2007 ALS artifacts and lack of access to raw 2007 data or processing information led us to decide that it was prudent to eliminate any possible vegetation-related influence on the VLM calculation. Accordingly, we concentrated our further analysis on the levee roads themselves. In general, levee roads are paved or gravel-surfaced and so no vegetation filtering is performed on them. This strategy was also in keeping with our principal objective of making VLM and overtopping projections for the structures most directly in contact with the Delta's river system.

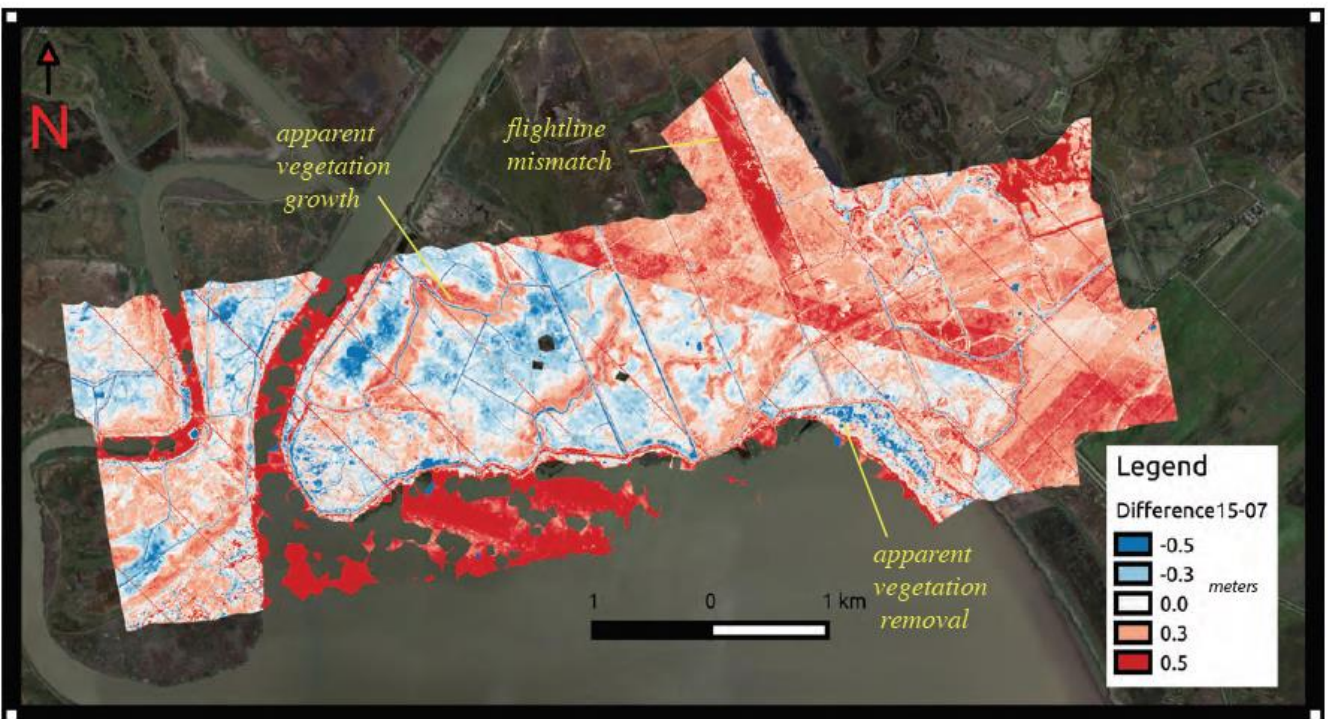


Figure 6. Vertical Land Motion (VLM) map of the Grizzly Island region (see Figure 1B for location) from 2007-2015. Positive VLM represents elevation gain, negative represents elevation loss. Identified features, described in the text, include vegetation growth, vegetation loss, and flightline mismatch.

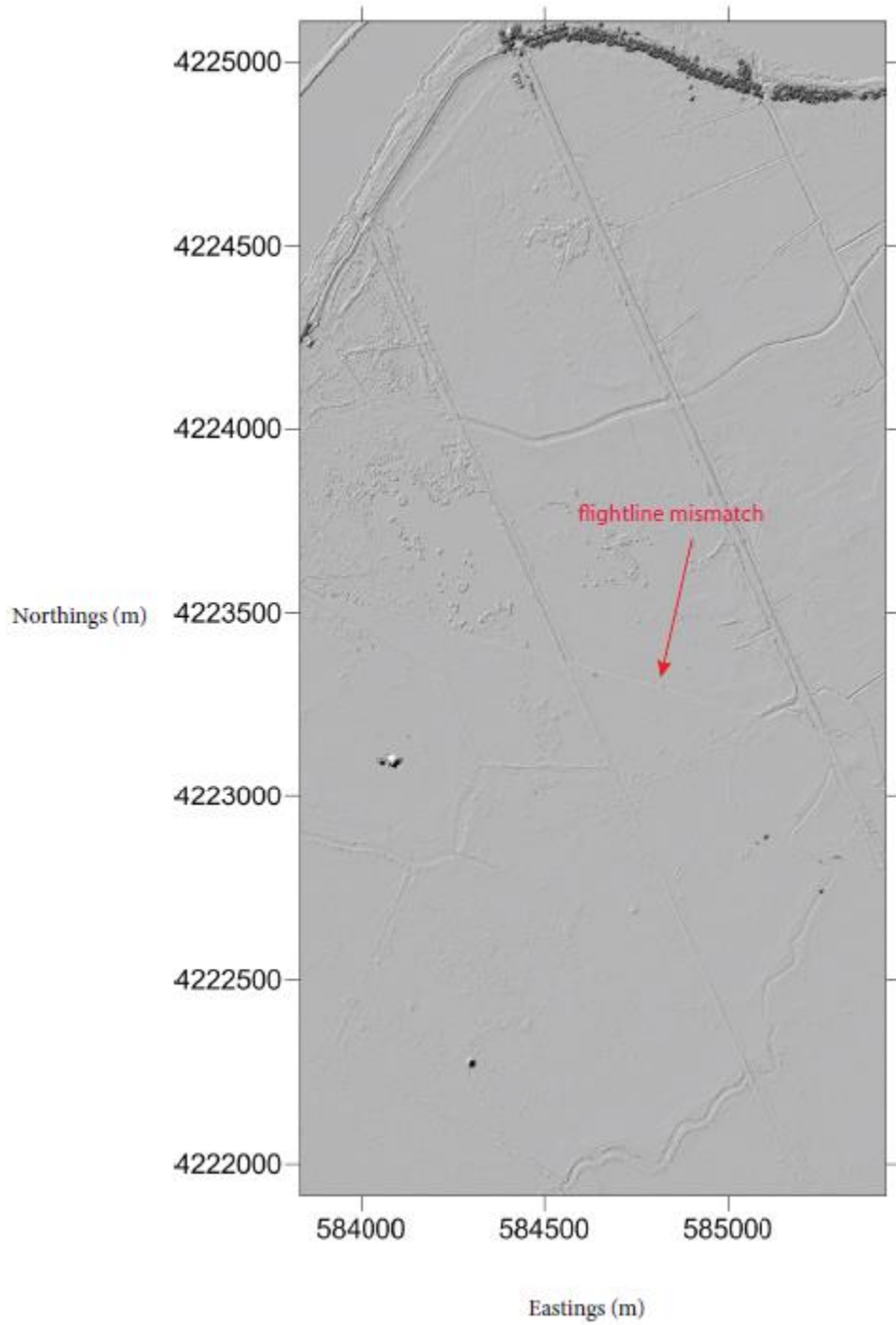


Figure 7. Shaded relief DEM (digital elevation model) of the 2007 ALS data set indicating a flightline mismatch.

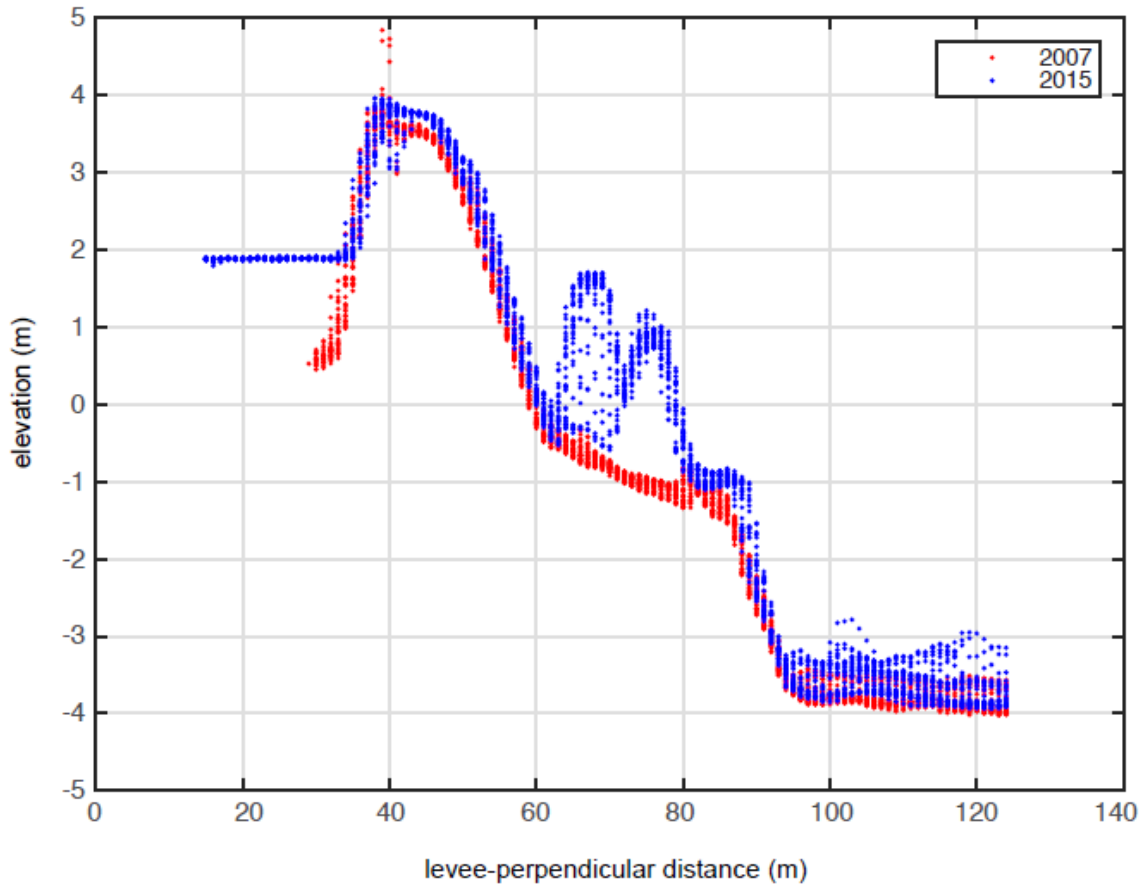


Figure 8. Example cross-section from a section of levee on Sherman Island. The lack of vegetated features in the 2007 data sets indicates the level of bare-earth filtering that was performed on it.

2.4.4 Levee Analysis

For the MLS datasets, following the data filtering, the MLS GNSS trajectories were used to define the location of the levee roads on all of the surveyed islands. We subdivided the datasets to reduce computational burden. Rather than using a random length, for example, every 500 m, the levee roads were subdivided using the maps of levee road health published by the Delta Stewardship Council (<http://deltacouncil.ca.gov/delta-maps>). The Delta Stewardship Council maps break the levee roads down into sections according to where work has been completed, where work needs to be done, and/or what levee flood standard (HMP or PL 84-99) the sections of road adhere to. After subdivision, a digital elevation model (DEM) Triangulated Irregular Network (TIN) was created for each dataset at the maximum resolution supported by the data. The TIN's provided a surface model from which elevation along the levee road trajectories could be output while minimizing interpolation. The MLS and 2015 ALS point cloud densities were both high enough to set a maximum edge length of 1 m for the near road triangulation. The 2007 ALS point cloud density was lower (< 1 point per m^2) and the maximum edge length

of the triangulation had to be set to 2 m. Typically, edge lengths were shorter than these threshold values, particularly in the area on or near the levee road surface, where MLS point cloud density was highest. A shorter TIN edge length provides higher resolution data over the road surface, which results in a more precise solution for levee VLM at that point. During the initial data filtering (2.4.1), terrain that diverged steeply from the road surface and had the potential to warp the road surface TIN near the road edges was removed from the data. Given that the road surface is wider than 2 m (the maximum on-road TIN edge length) and that the filtering removed features that abruptly altered the near-road elevation, the final road surface triangulation along the MLS trajectory, which was typically at or near the road center, was not warped by changing elevation off the road surface

For the ALS dataset covering Grizzly Island and parts of Sherman Island, no MLS trajectories were available (because the data were being collected from the air, we did not drive them). Because the MLS trajectory could not be used to define the levee road around Grizzly Island, the topographic feature created by the road surface itself was used instead. We created an unfiltered DEM for each ALS point cloud along the road surface. The Delta Stewardship Council has not published a levee road health map for Grizzly Island so the road surface was output as a single segment and then divided into multiple ~1000 m sub-segments for analysis and plotting. Most of the remaining two thirds of Sherman Island meet the PL84-99 standard so the ALS – ALS comparison on Sherman Island was also divided into 1000 m segments for analysis and plotting.

2.5 Water Level Projection: Sea-Level Rise and 100 Year Flood Stage Height

In order to estimate the water level contribution to overtopping, we consider two components: 1) future Sea-level rise (SLR) and 2) the 100-year flood stage height.

For the first component, we assumed that SLR projections for San Francisco would be valid upstream in the Delta. There is ~80km of water pathway between the Golden Gate Bridge and the westernmost Delta Islands. We accept that there are hydrodynamic processes associated with the combined river & estuary system that will cause differences in sea-level between the Delta and the open ocean. For the purposes of this study, however, we consider those effects negligible. For SLR estimates at San Francisco, we take the end-member scenarios of the suite of scenarios considered for the recent 4th California Climate Assessment (Cayan, Kalansky et al. 2016). Specifically, we choose the 50th and 99th percentile solution for the RCP4.5 and RCP8.5 scenarios, respectively, as a reasonable range of scenarios (Fig. 9).

For the second component, we assigned the 100 year flood stage height for each VLM location by performing nearest-neighbor interpolation of 24 gaging stations throughout the Delta for which the Army Corps of Engineers estimated 100 year flood stage (Fig. 10) (Department of the Army 1976).

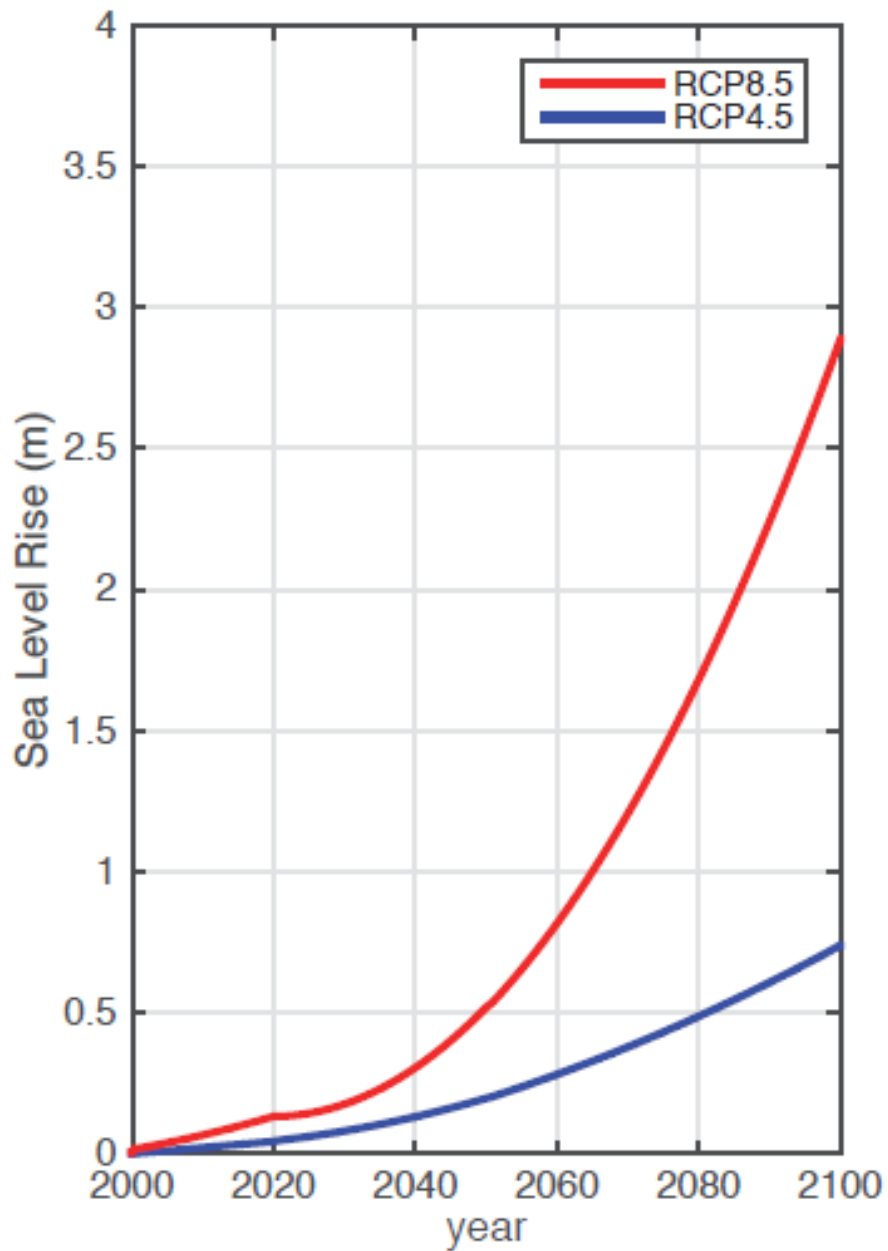


Figure 9. Range of SLR (sea-level rise) projections used in this study from *Cayan et al, 2017*. In order to capture a conservative range of the projections, we use the RCP, representative concentration pathways, for a fast (RCP 8.5, 99% percentile) and slow (RCP 4.5, 50% percentile) scenario.

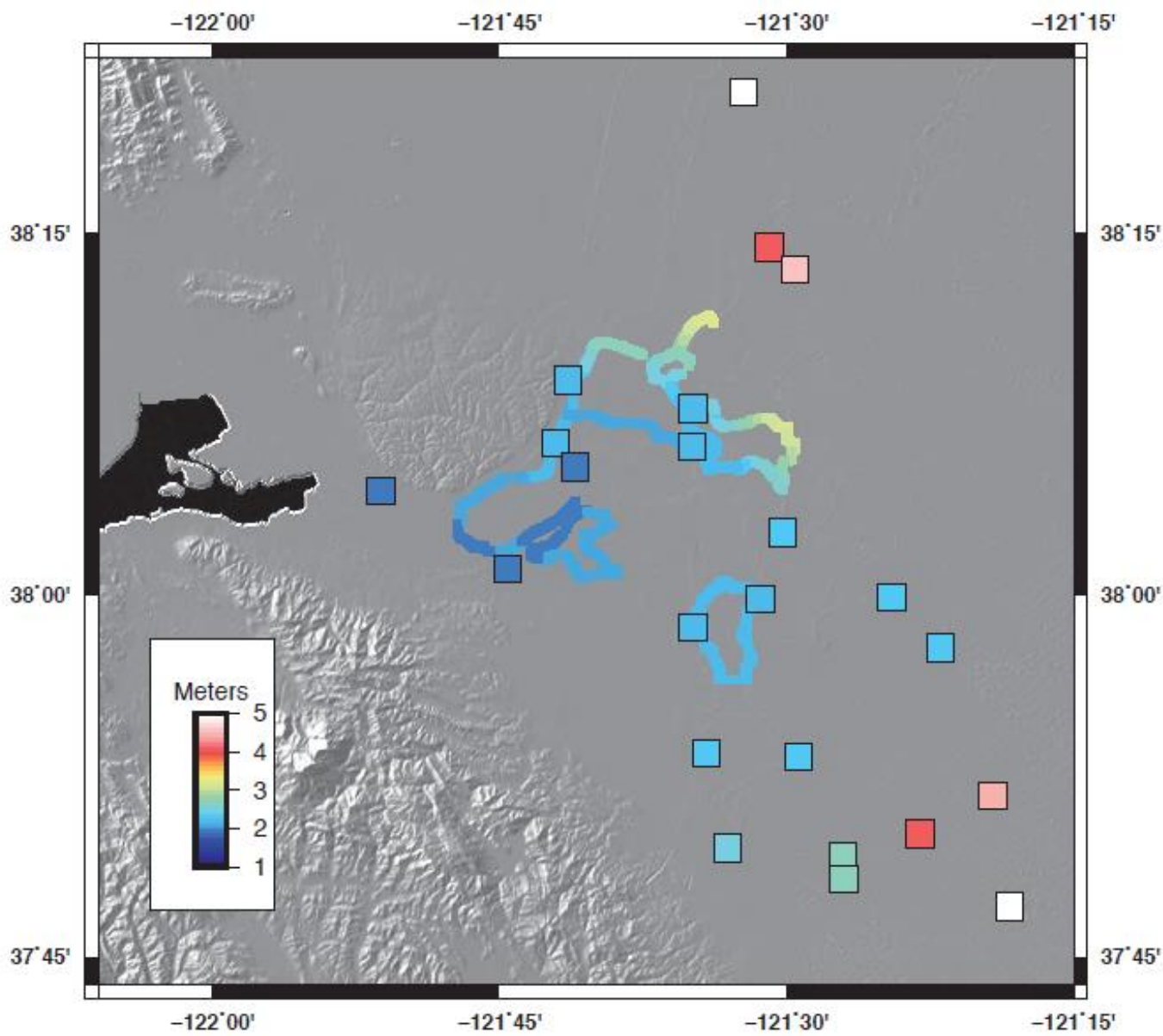


Figure 10. Map of the Delta with gauging stations (large colored squares) used by the Army Corps of Engineers for its 100-year flood stage projections. The colored line represents the nearest-neighbor interpolation of the 100 year flood estimates for levee locations where we made VLM estimates.

2.6 Overtopping Projection

In order to project when a section of levee will fall below the PL84-99 flood standards we consider the following equation:

$$u_0 + VLM \cdot t = SLR(t) + u_{100yr} + u_{pl84-99} \quad (1)$$

where, for each measurement point, u_0 is the elevation for the last measurement epoch (meters), VLM is the linear subsidence rate (meters/year), t is time (years), u_{100yr} is the 100 year flood stage height elevation, and $u_{pl84-99}$ is the constant PL 84-99 threshold value (0.4572 meters).

The left-hand side of eq. 1 is a straight line with a negative slope (we are only considering subsidence, $VLM < 0$) and the right-hand side is the same as the sea-level projection curves (Fig. 9), offset vertically by the spatially variable values of u_{100yr} (Fig. 10) and the constant value of $u_{pl84-99}$ (Fig. 11). For each levee position we find exceedance date, t_e , the date when the left-hand side of equation (1) first drops below the right-hand side.

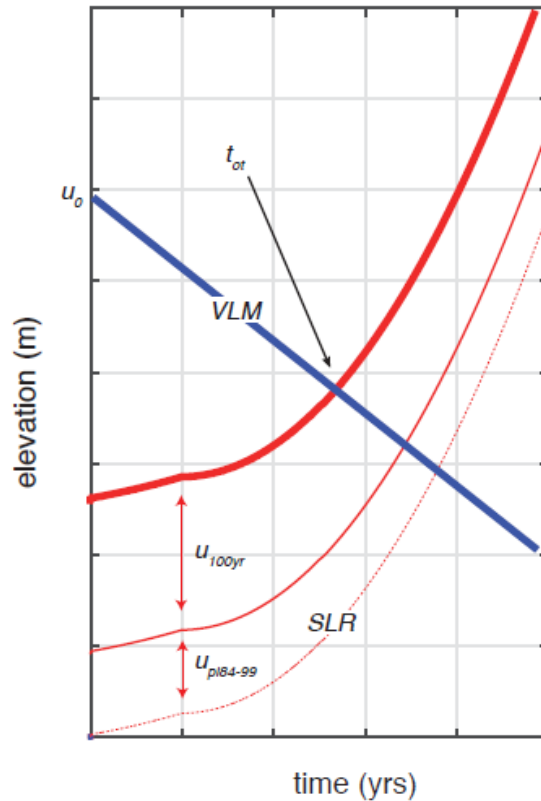


Figure 11. Schematic of how the overtopping exceedance date projection is calculated. Blue line, linear VLM trend starting from initial elevation (u_0). Thick red line, SLR projection (same as Figure 9), with the constant values of $u_{pl84-99}$ and u_{100yr} added. When the thick red line exceeds the blue line at the exceedance time, t_e , the levee will be overtopped.

3: Results

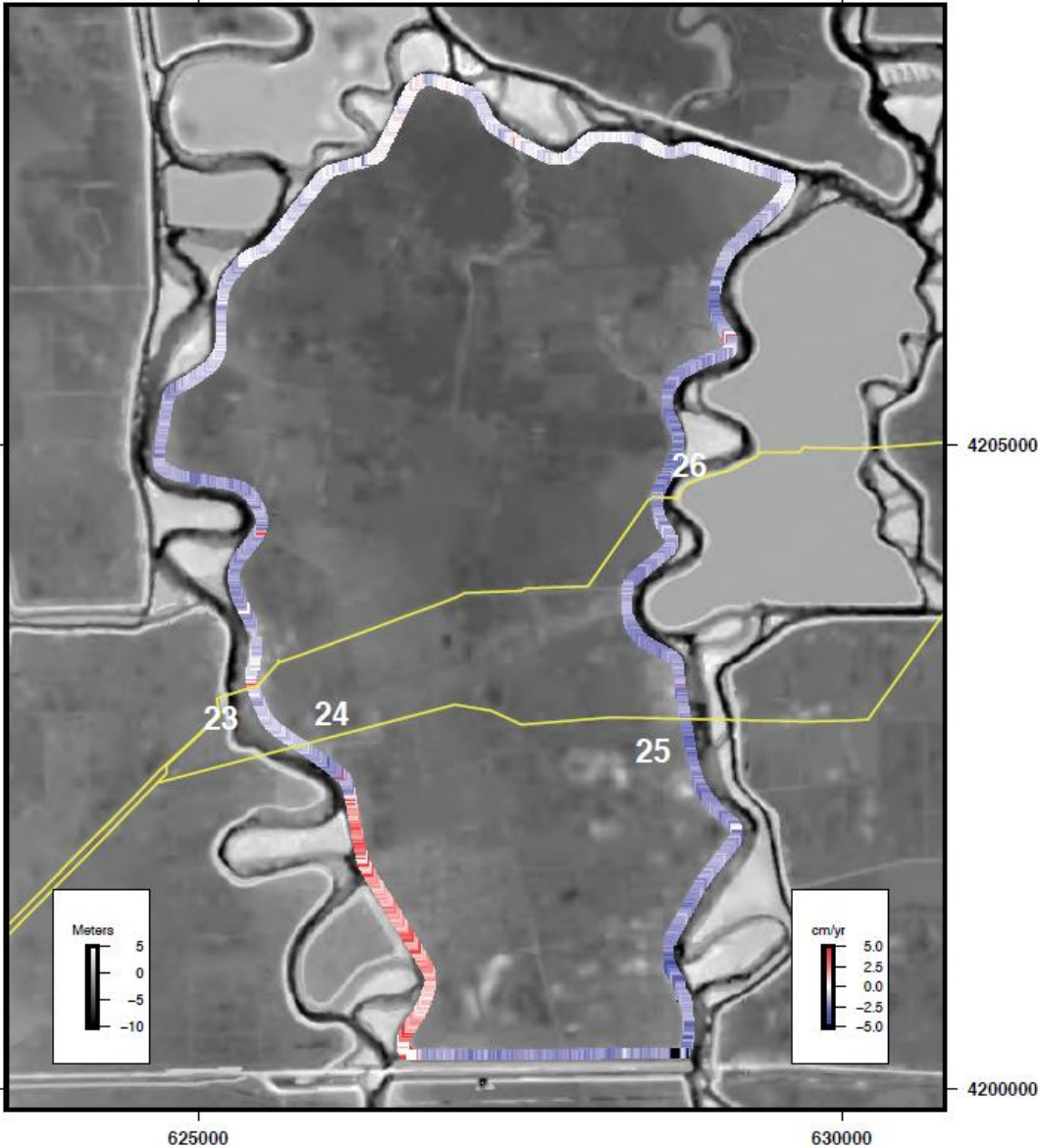
3.1 Gross VLM & Anthropogenic Signal

For completeness we present all of the VLM estimates, what we term "gross" VLM, because positive VLM values are included. There are no natural physical processes known to us that would occur in the Delta to create such large positive VLM changes parallel to levee crests over 10s to 100s of meters length scales. Neither seasonal aquifer recharge (Brooks, Bawden et al. 2012) nor seasonal regional uplift in the Sierra Nevada close to the Delta's eastern margin (Amos, Audet et al. 2014, Hammond, Blewitt et al. 2016) varies over the much shorter spatial scales of the Delta levees. Similarly, levels of microseismicity and tectonic activity in the Delta are not sufficient to create measureable VLM signals (Brooks, Bawden et al. 2012, Brooks and Majunath 2012). Accordingly, we are confident in attributing the majority of these positive VLM values to anthropogenic effects, primarily levee repairs and road leveling (see below). In general, VLM values range from $\sim -5\text{cm/yr}$ to $+10\text{cm/yr}$ (Figs. 12a-f).

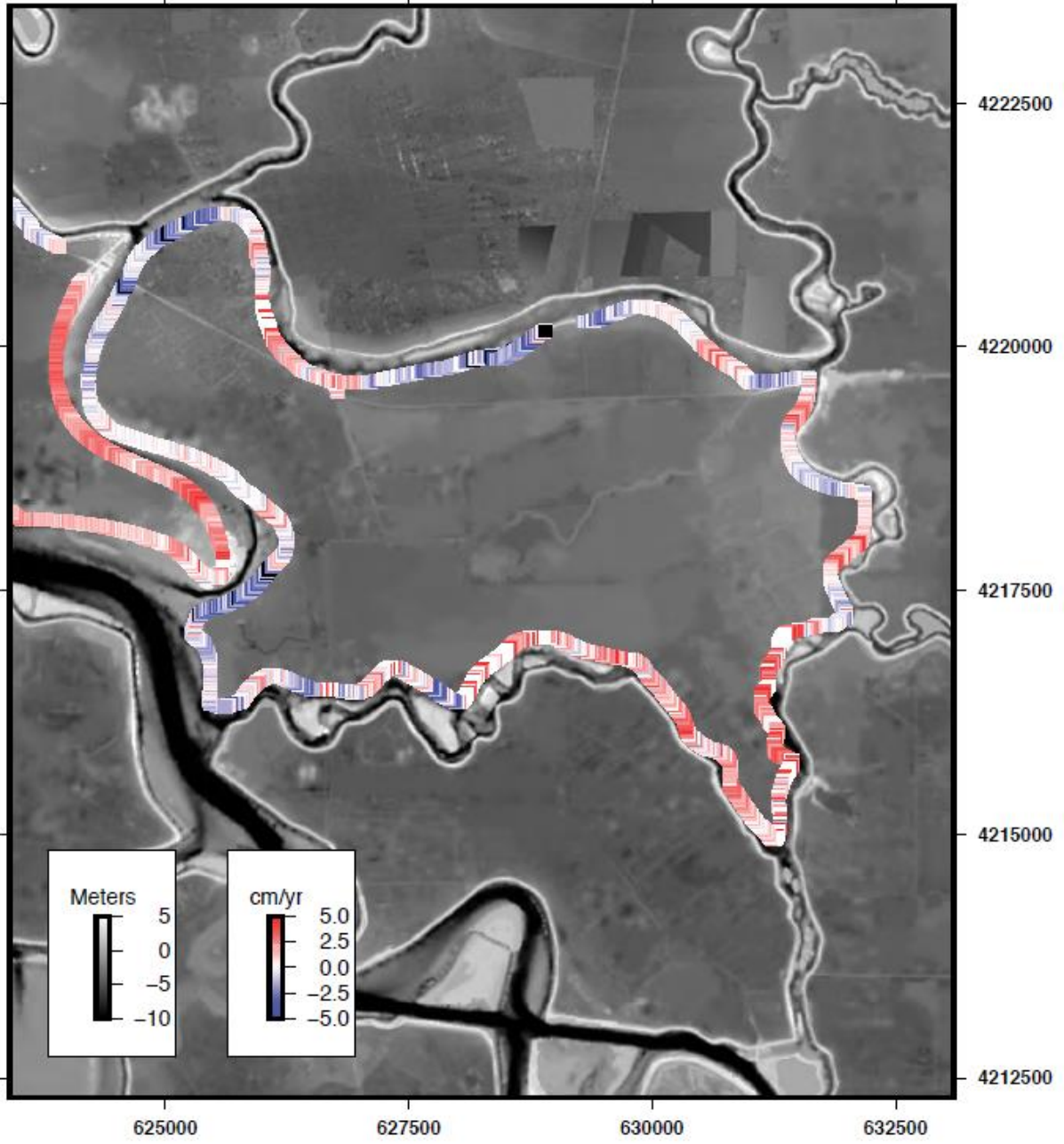
In Figure 13 we plot initial elevation versus gross VLM for all datasets collected and see that there is a distinct correlation (linear relationship with slope of ~ -1) between the two in some portions of the data. For positive gross VLM this correlation is clearly associated with post-2007 levee road filling to a constant level (Fig. 14). Simple consideration of raising an initially variable elevation profile to a constant value will lead to a relation between initial elevation and gross VLM of -1 . For negative gross VLM the correlated datasets are associated with planning off and filling of levee roads (Fig. 15). As lower sections of levee road are filled in, some areas are also lowered so a levee road that previously had local highs and lows is leveled. This will also create a slope of -1 relating initial elevation and gross VLM. Because these anthropogenic VLM values are related strictly to one-time road repairs, we identify the affected datasets using the correlation plots and remove them from any subsequent analysis.

Figure 12a-f. Gross VLM plots for each of the studied regions (colored-squares; black where negative rate is lower than minimum value in color scale). Base map (grey-scale) is the 2007 ALS data set in UTM Zone 10 projection. Yellow lines, natural gas pipelines. White numbers indicate the index, assigned by this study, of a specific pipeline crossing (see Figure A1). See Figure 1B for locations. All data are second acquisition minus first acquisition, where the first acquisition is the 2007 ALS data set. Second acquisition type indicated in parentheses. A) Bacon Island (MLS). B) Bouldin Island (MLS). C) Grizzly Island (ALS). D) Isleton/Andrus/Brannon Islands (MLS). E) Jersey Island (MLS). F) Sherman Island (ALS).

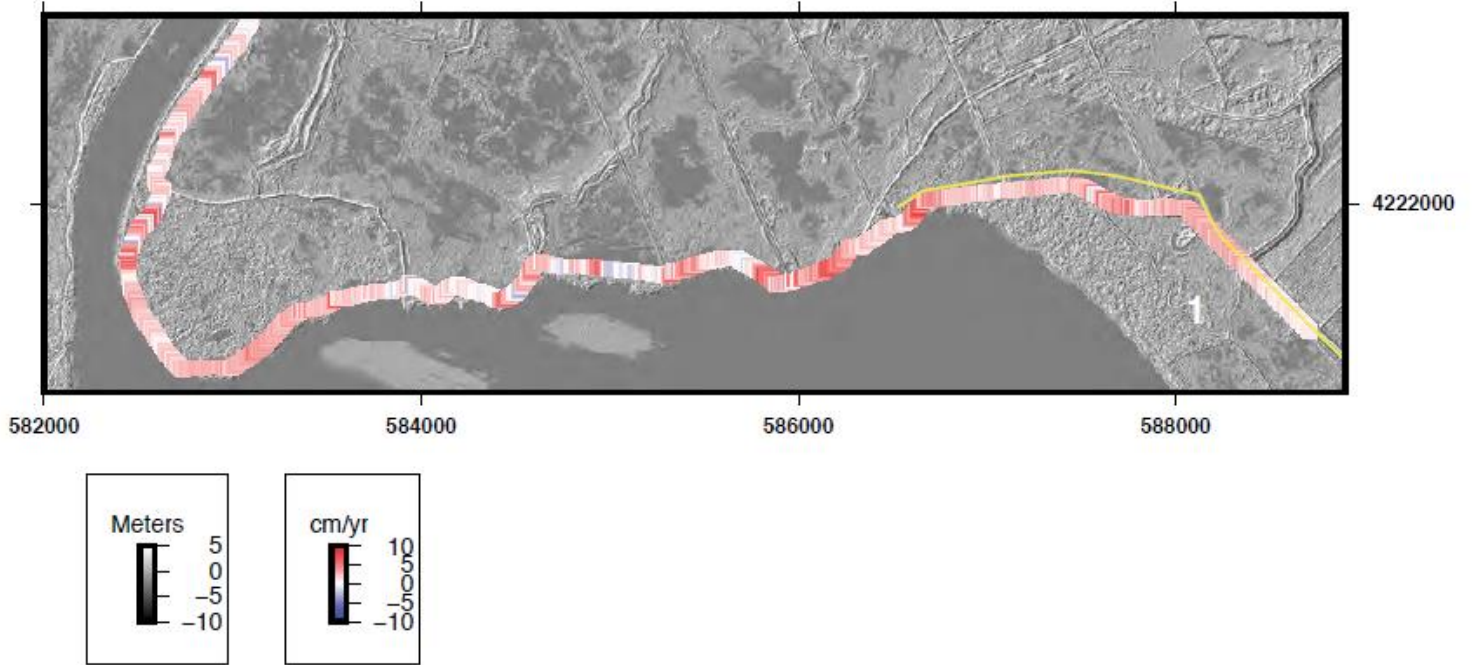
Bacon Island VLM



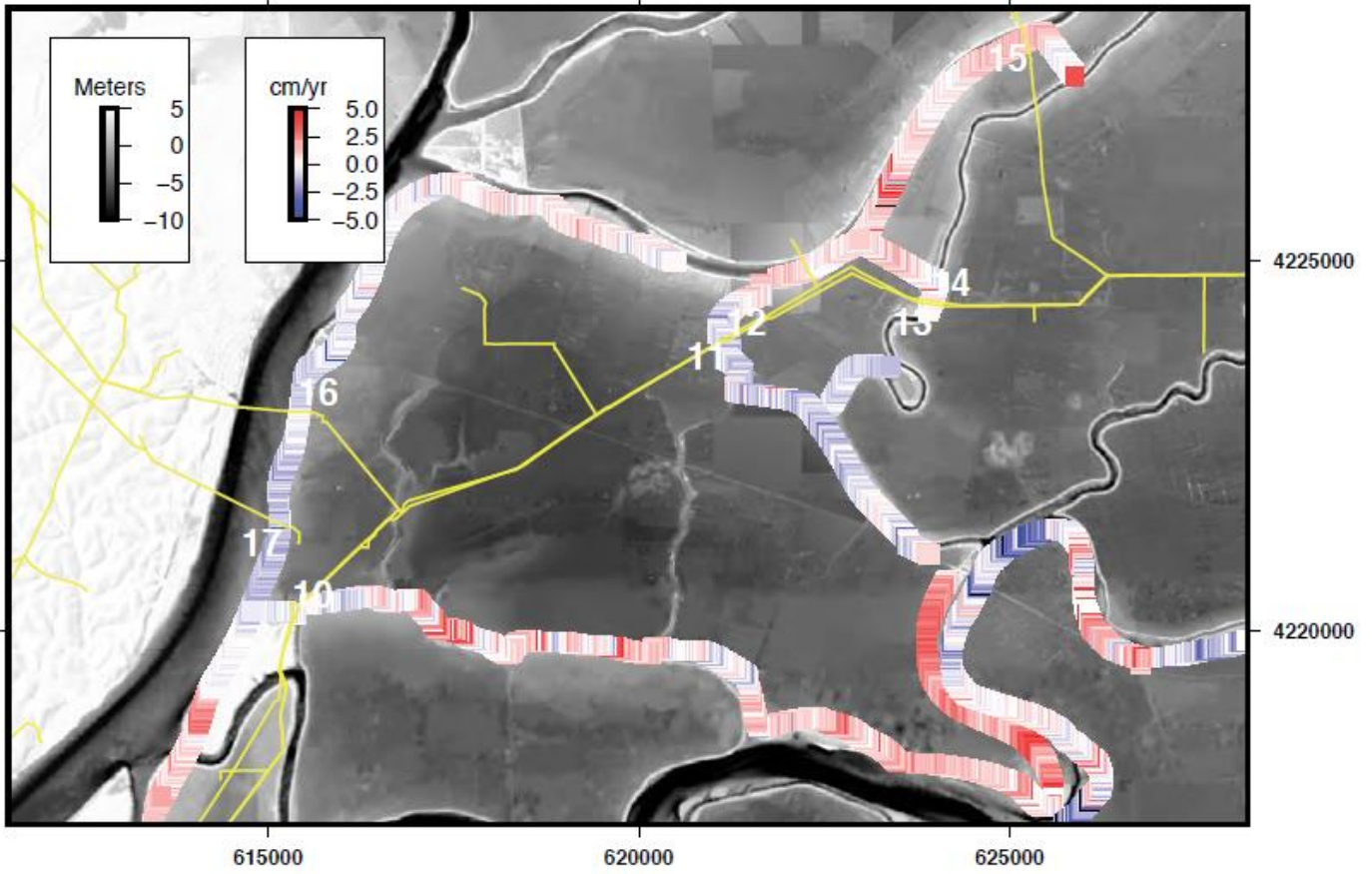
Bouldin Region VLM



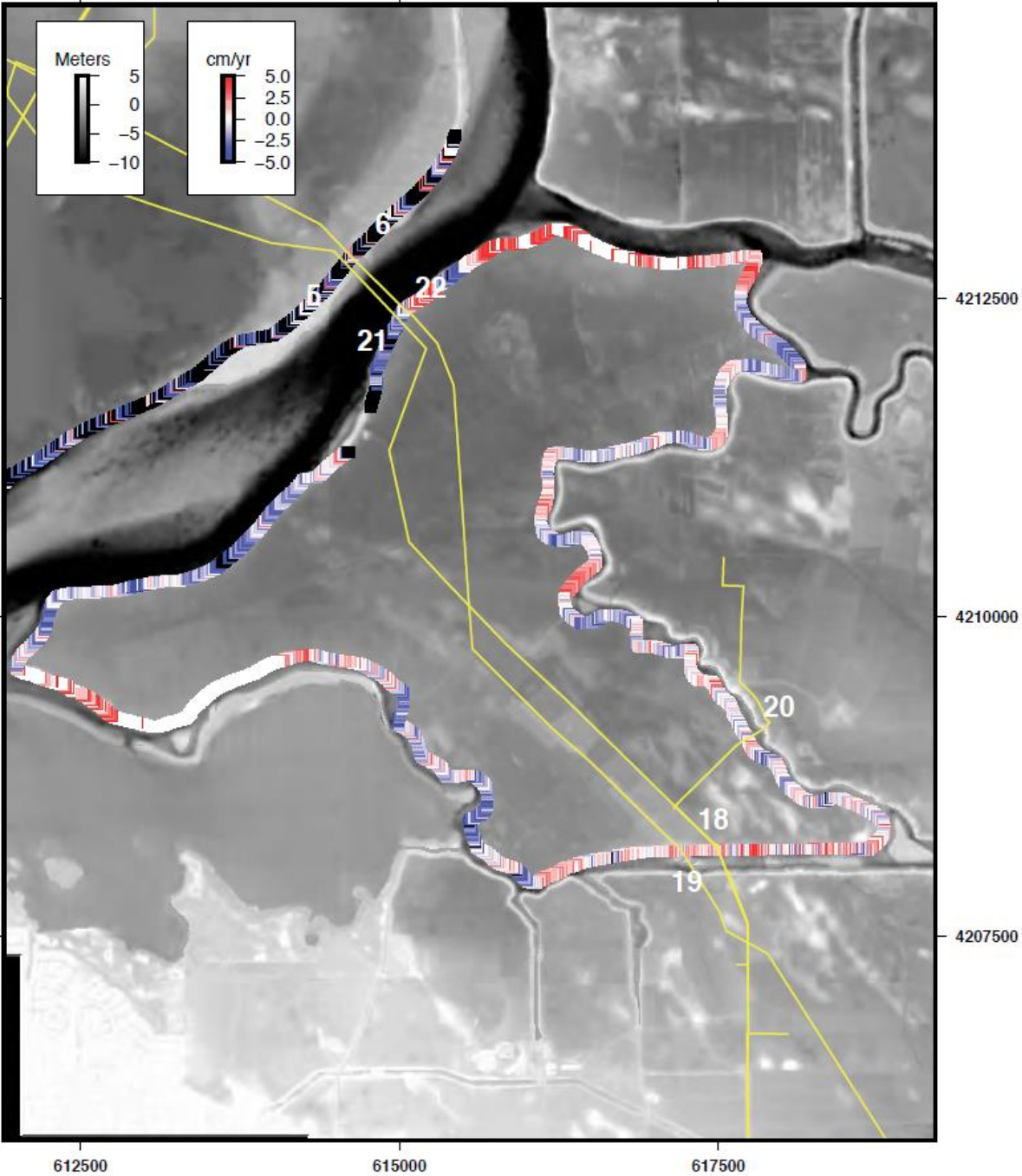
Grizzly Region VLM



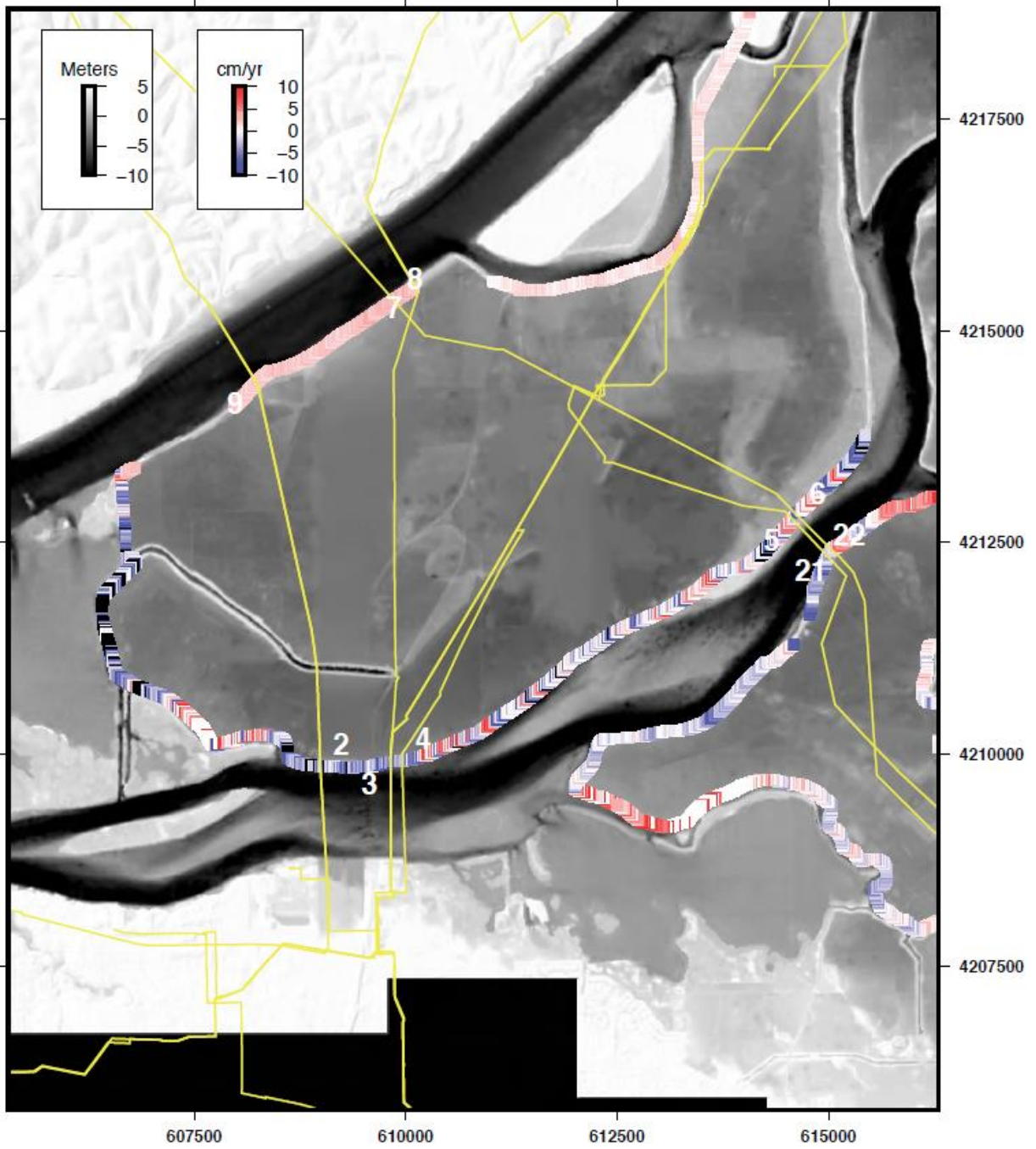
Isleton Region VLM



Jersey Region VLM



Sherman Region VLM



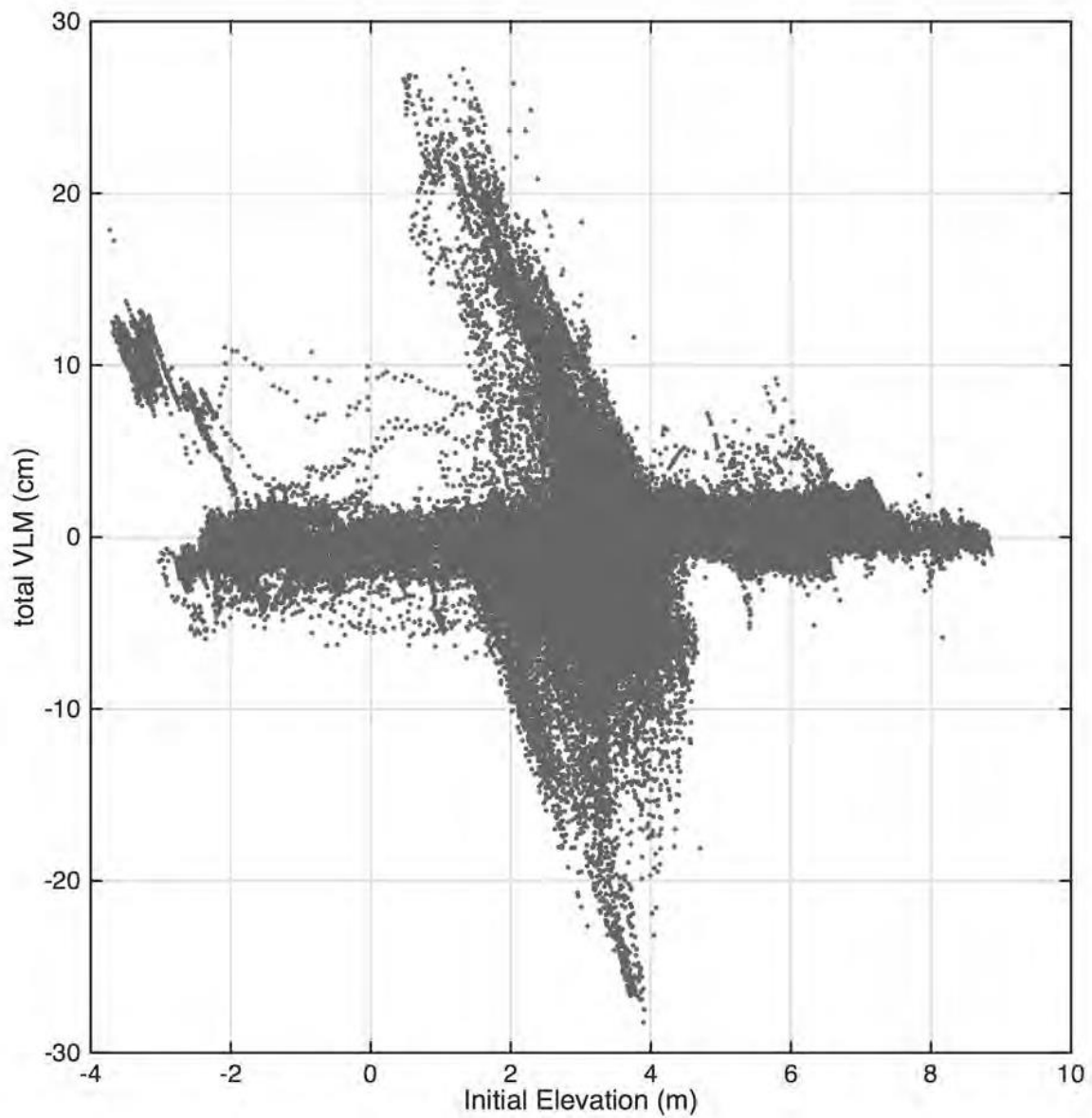


Figure 13. Plot of all data in the Delta showing negative correlation for some locations between initial elevation and total VLM (not rate).

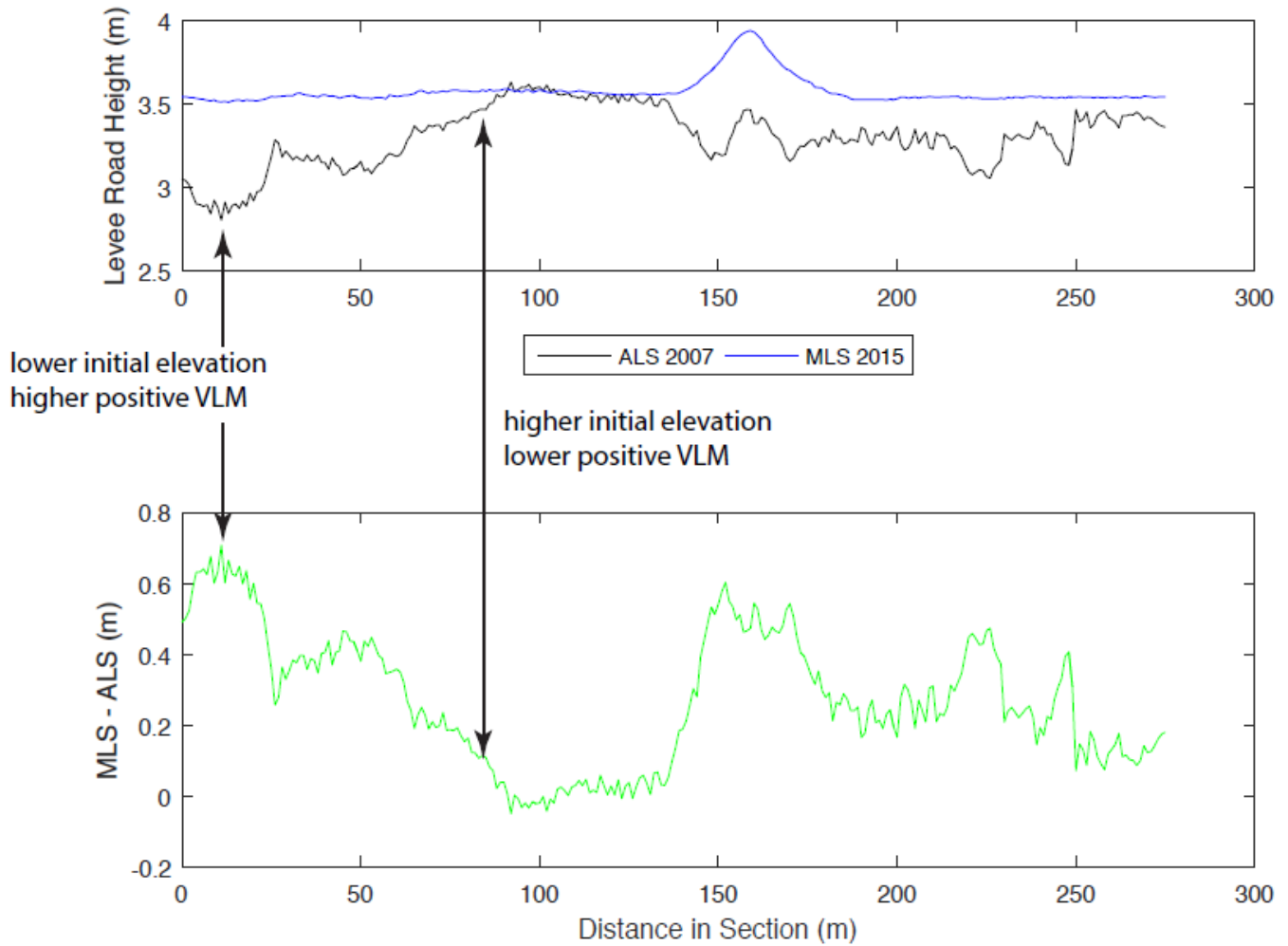


Figure 14. Example of a segment of levee showing both acquisitions of data and how apparent road remediation (filling and leveling) contributes to the correlations demonstrated in Figure 13.

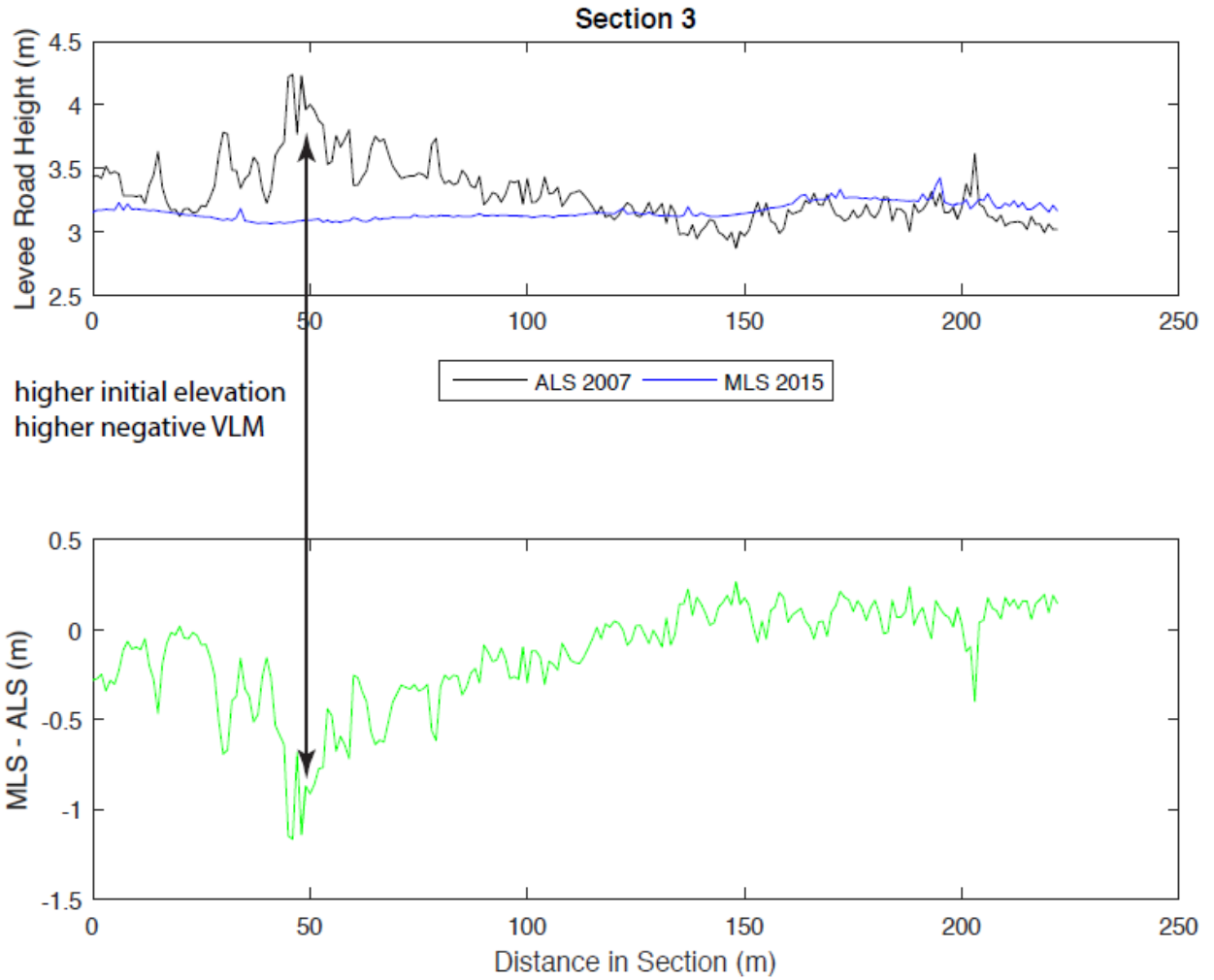


Figure 15. Example of a segment of levee showing both acquisitions of data and how apparent road remediation (cutting and leveling) contributes to the correlations demonstrated in Figure 13.

3.2 Subsidence

In this section we present only locations with negative VLM (subsidence) that have not been contaminated by the anthropogenic effects described above. We present the VLM data as a series of maps for the sub-regions studied (Fig. 16a-f). In each of the maps we also identify the natural gas pipeline crossings (white numbers in Fig 16a-f, see discussion below). To characterize general trends we also present histograms of VLM values for the sub-regions (Fig. 17). Generally, subsidence varies between 0-5cm/year (Fig. 17). 5 of the 6 histograms have mean subsidence values on the order of ~ 0.75 -1.5 cm/yr. The Sherman Island region has a notably broader histogram with a mean of ~ 5 cm.

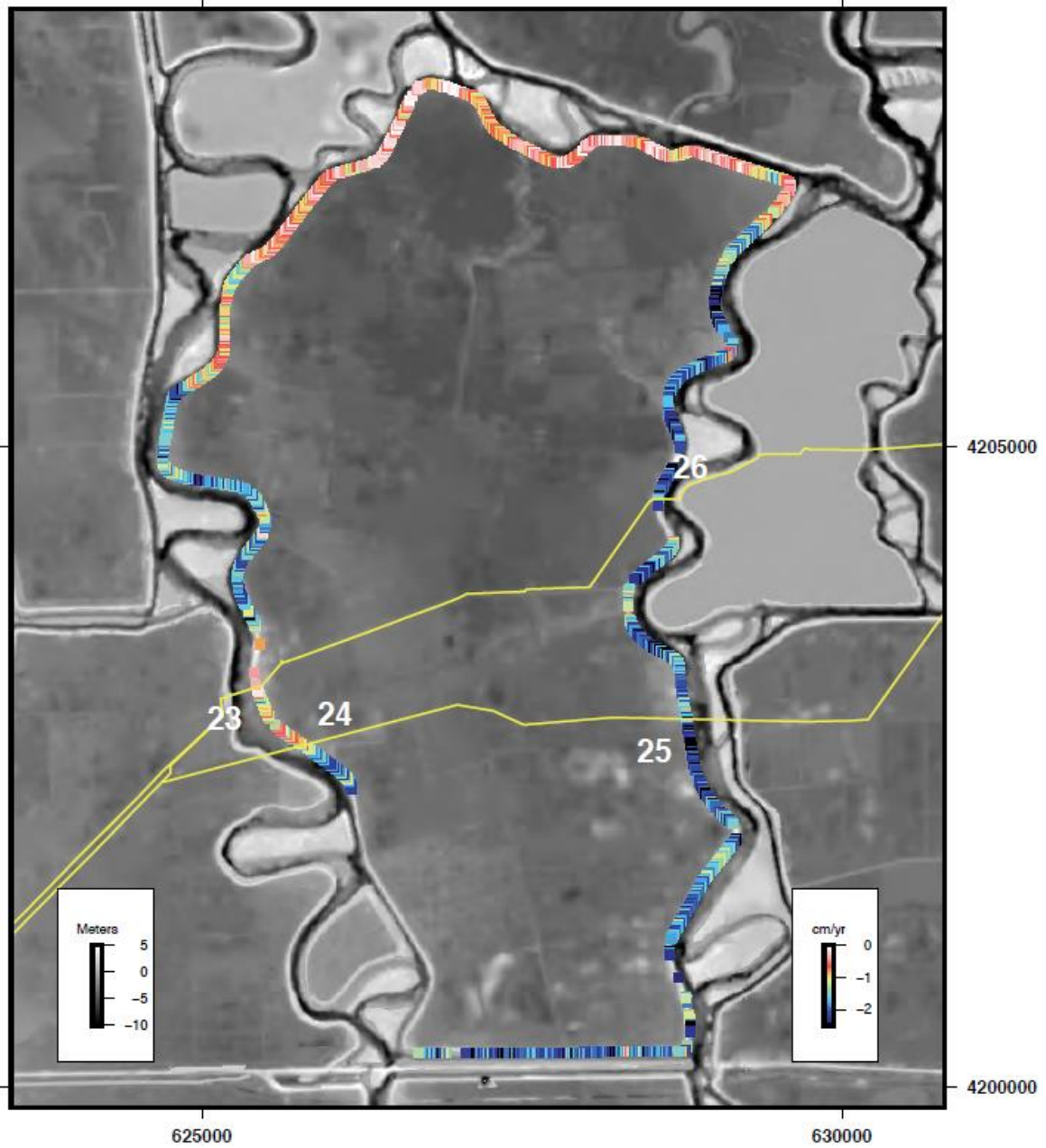
Examining the sub-regions more closely we see that levee-crest parallel gradients in VLM can be on the order of cms over distances of meters (Fig. 16a-f). For the Isleton sub-region it appears that the southern portion is subsiding at ~ 0.5 cm/yr in comparison to the western portion at ~ 2 cm/yr. For the Bacon sub-region the northern portion of the island appears to be subsiding at ~ 0.5 cm/yr compared to the rest of the island which is subsiding at ~ 2 cm/yr. The Jersey sub-region is subsiding most at ~ 0.5 cm/yr except for very localized patches (see pipeline crossing discussion below). The Bouldin sub-region subsides in a fairly uniform manner at rates close to the ~ 1 cm/yr mean rate.

For each of the pipeline crossings, we analyze subsidence within a 100 meter region centered on the pipeline crossing (Fig. A1 in Appendix A). Because the VLM gradients can vary rapidly in space it becomes immediately apparent that local analyses are required for pipeline-specific analyses are required.

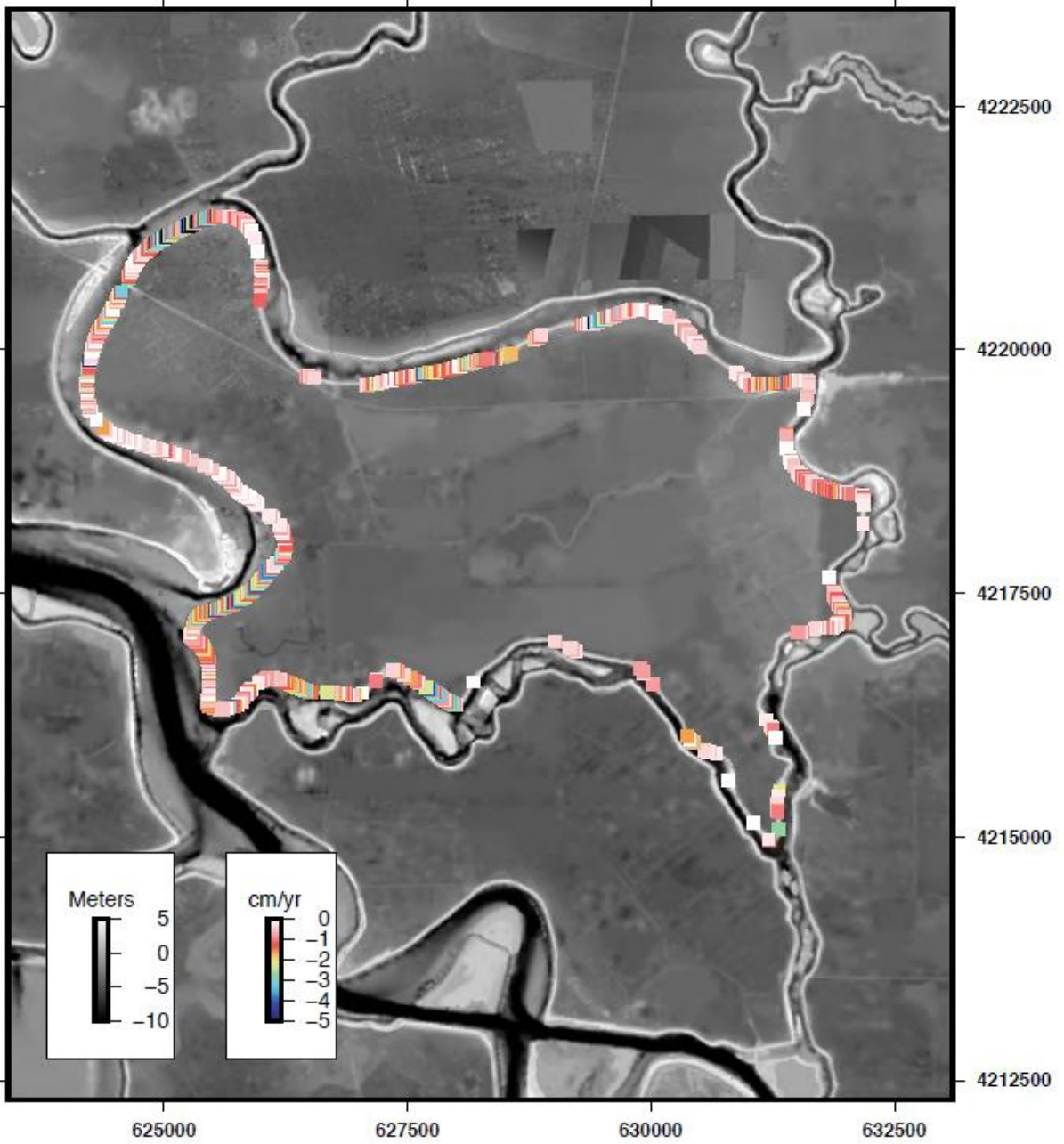
For the Jersey sub-region all of the crossings exhibit VLM values similar to the island-wide trends except for crossing #21. For the Bacon sub-region the eastern crossing (# 25 and 26) exhibit VLM rates of ~ 2 cm/yr whereas the western crossings (#23 and 24) have a rate of ~ 1 cm/yr. The Isleton sub-region is an example of how strongly VLM rates can vary with distance. Crossing #10 has a VLM rate of ~ 0.5 cm/yr whereas only ~ 500 m to the northwest, crossing #17 has a rate of ~ 2 cm/yr. Crossing #17 further shows an increase in subsidence rate towards the crossing itself from ~ 1.5 cm/yr to a maximum of ~ 2 cm/yr closest to the crossing location itself.

Figure 16a-f. Final VLM plots for each of the studied regions, identical to Figure 12 A-F, except that zones of positive VLM have been removed to highlight subsidence. See Figure 1B for locations. All data are second acquisition minus first acquisition, where the first acquisition is the 2007 ALS data set. Second acquisition type indicated in parentheses. A) Bacon Island (MLS). B) Bouldin Island (MLS). C) Grizzly Island (ALS). D) Isleton/Andrus/Brannon Islands (MLS). E) Jersey Island (MLS). F) Sherman Island (ALS).

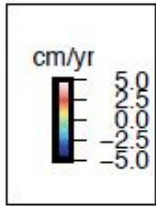
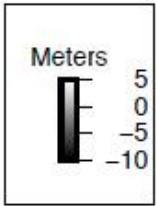
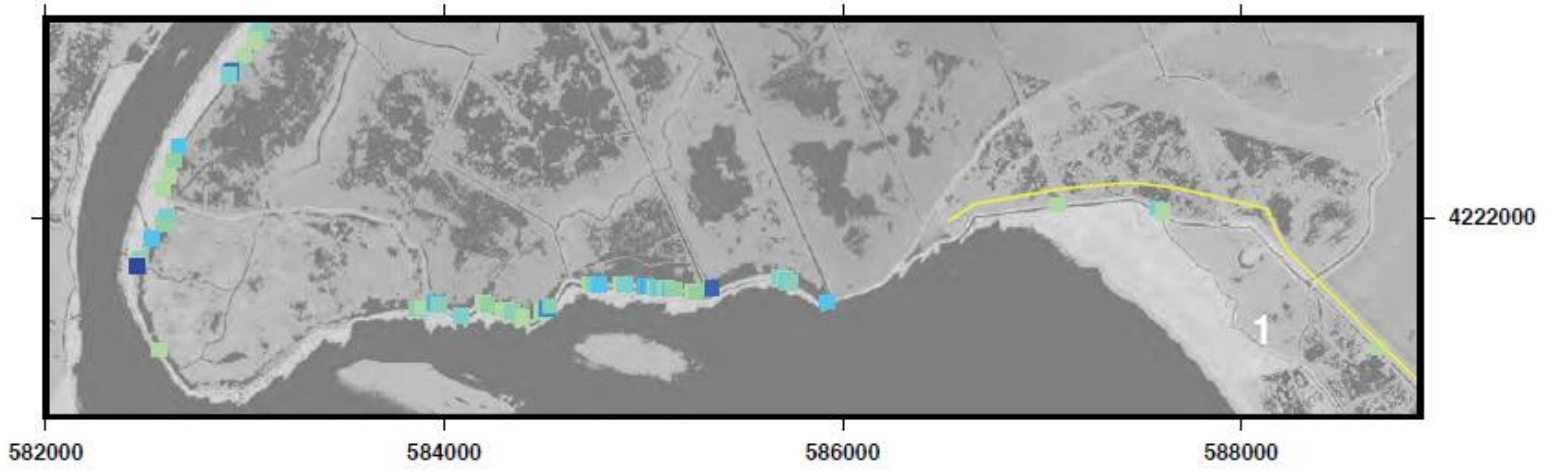
Bacon Island VLM



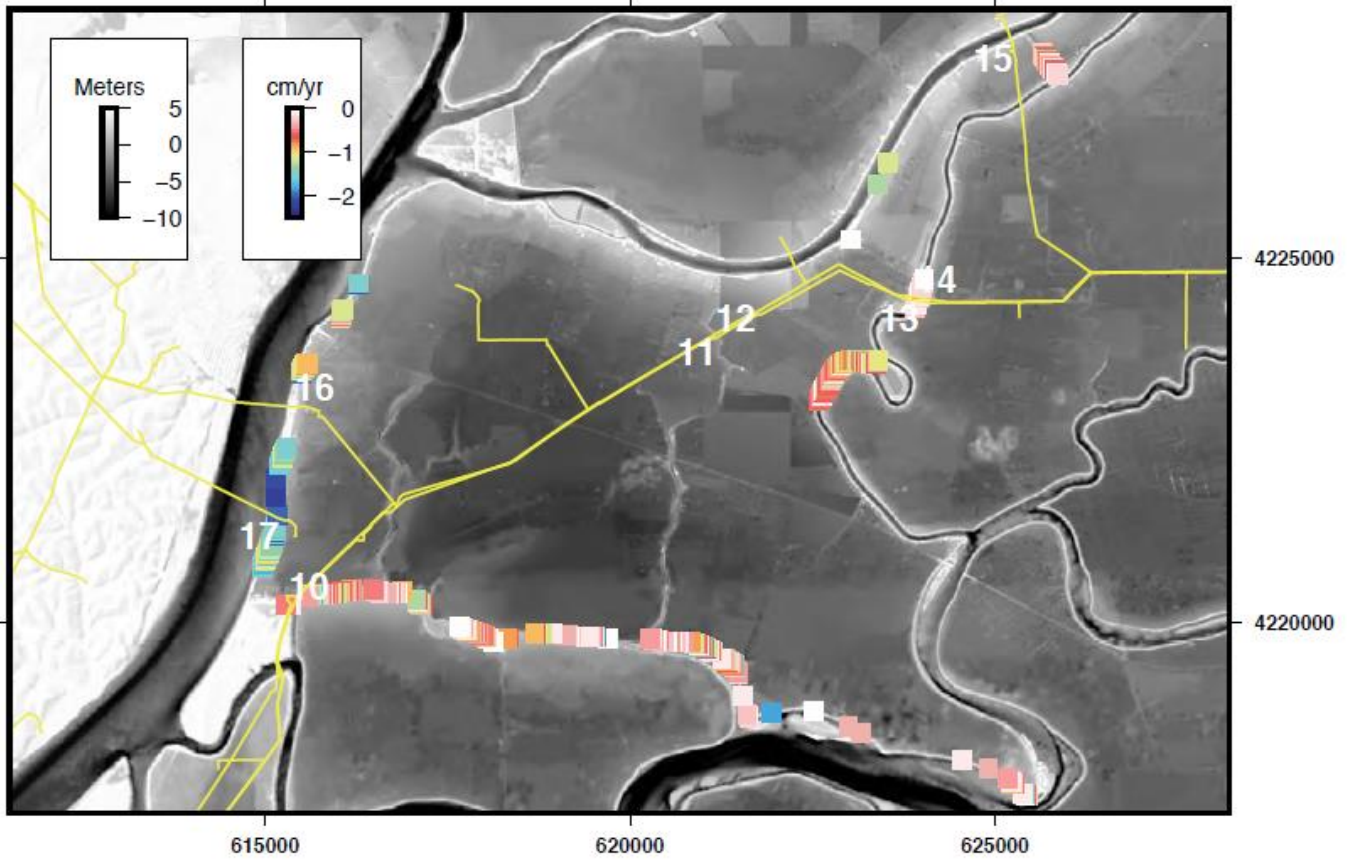
Bouldin Region VLM



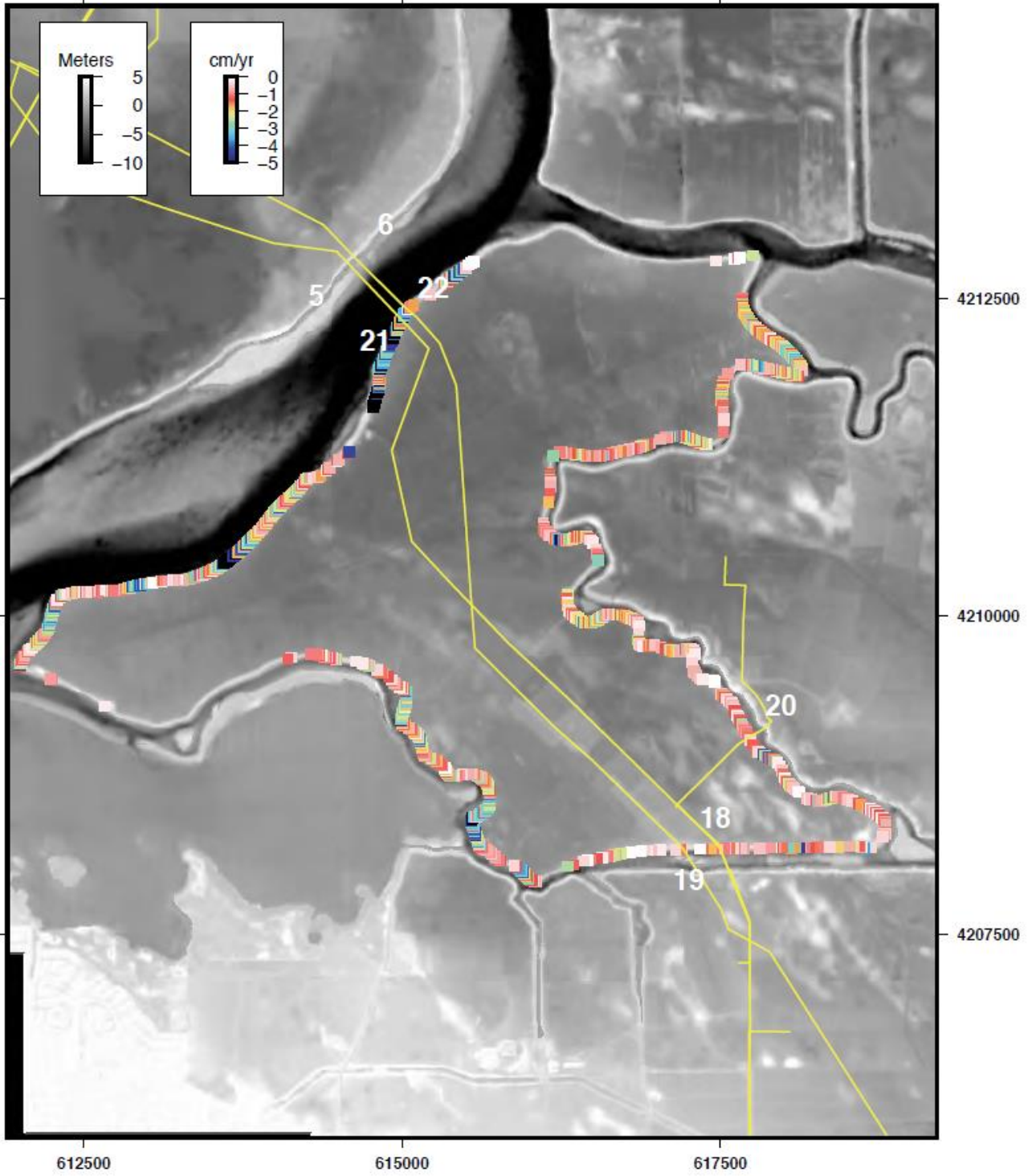
Grizzly Region VLM



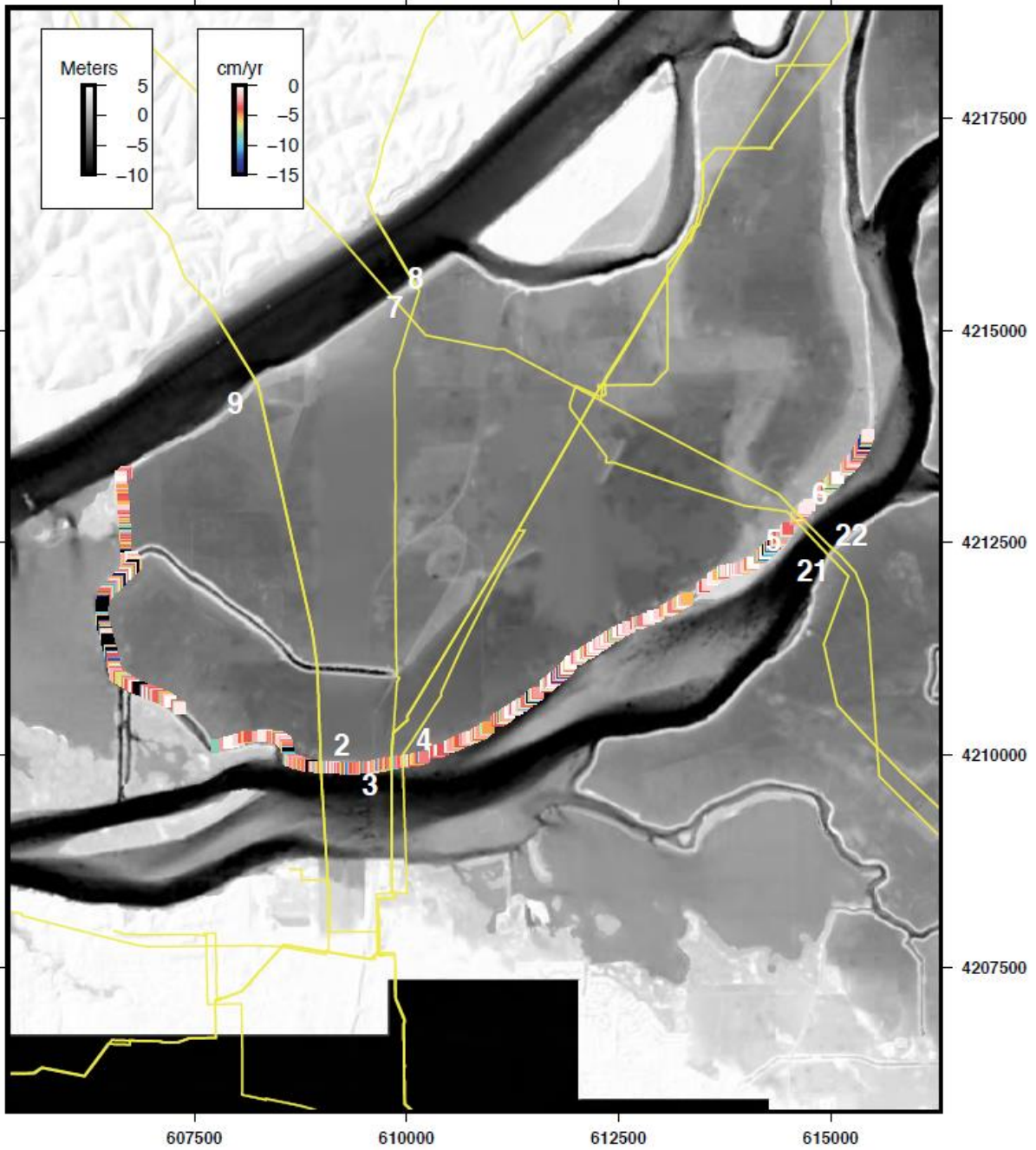
Isleton Region VLM



Jersey Region VLM



Sherman Region VLM



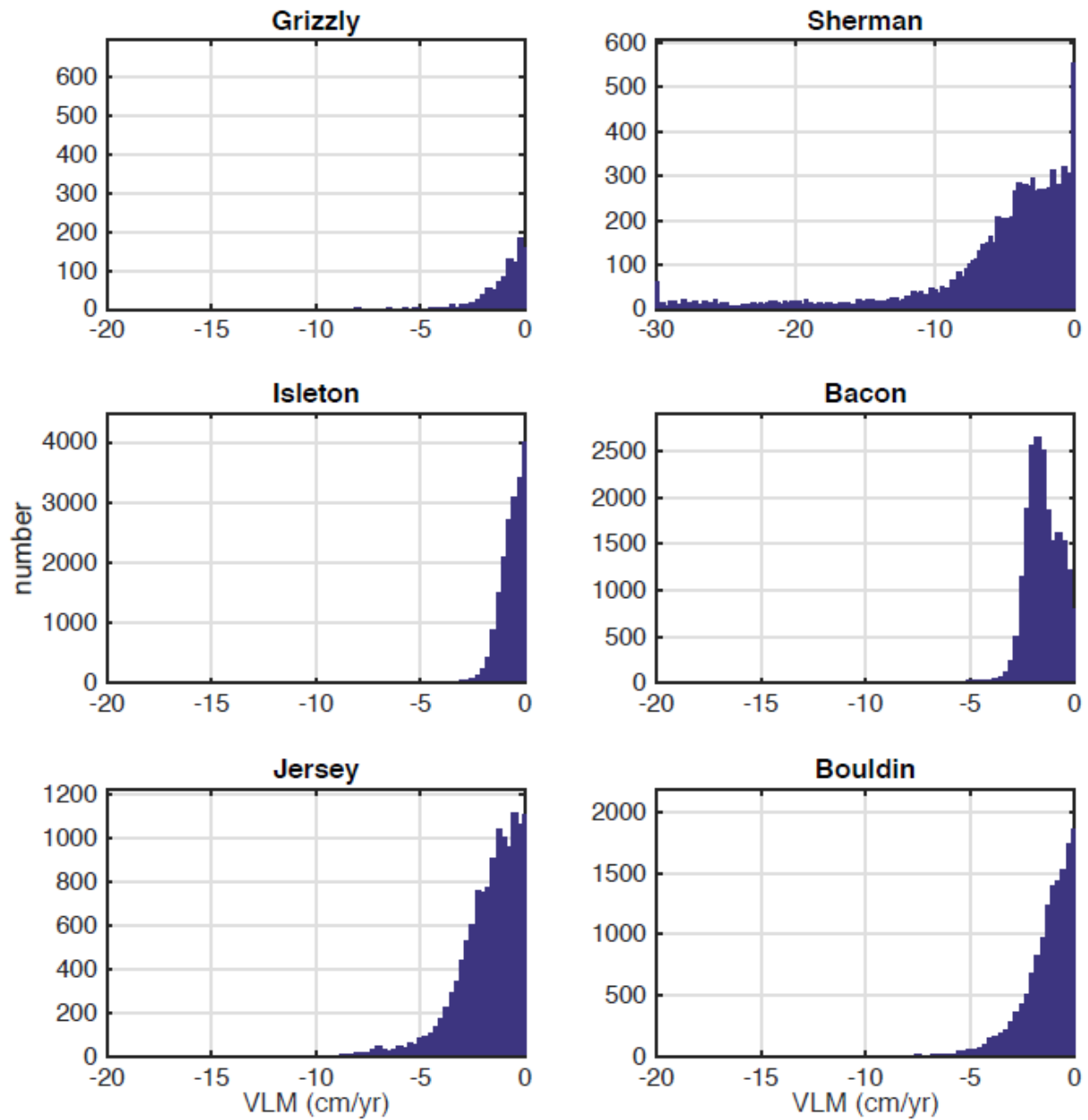


Figure 17. Histogram, for each island region studied, of subsidence rate.

3.3 Overtopping Projections

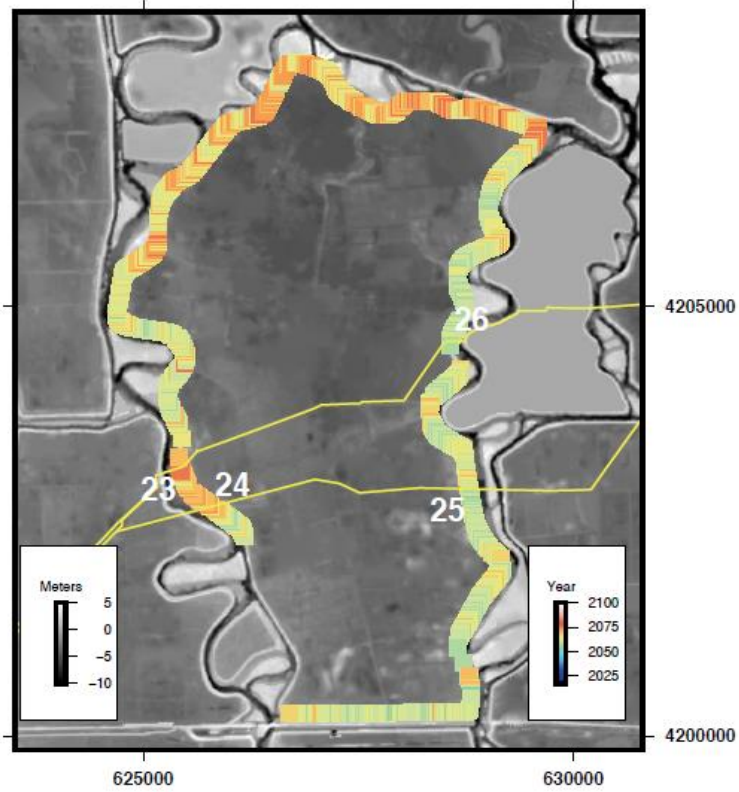
In order to present a conservative analysis, we present overtopping projection results using a range of SLR projections from RCP 8.5 99% ("fast SLR") and RCP 4.5 50% ("slow SLR"). As with the VLM projections, we present both general and sub-region specific maps (Fig. 18a-e). Because there are so few LIDAR reflections from the levees in the Grizzly dataset we do not present overtopping projections for it.

Generally, four of the sub-regions (Bacon, Bouldin, Jersey, and Isleton) have modal dates of threshold exceedance of ~2060 and 2080 for the fast and slow SLR cases, respectively (Figure 19). The Sherman sub-region has modal exceedance dates of ~2045 for both cases (Figure 19). Because SLR is constant for the whole Delta at any given point in time, the difference in the shape of the Sherman histogram for the two cases is a representation of the variability in the estimation of the 100-year flood height estimation for Sherman Island (see Figure 10).

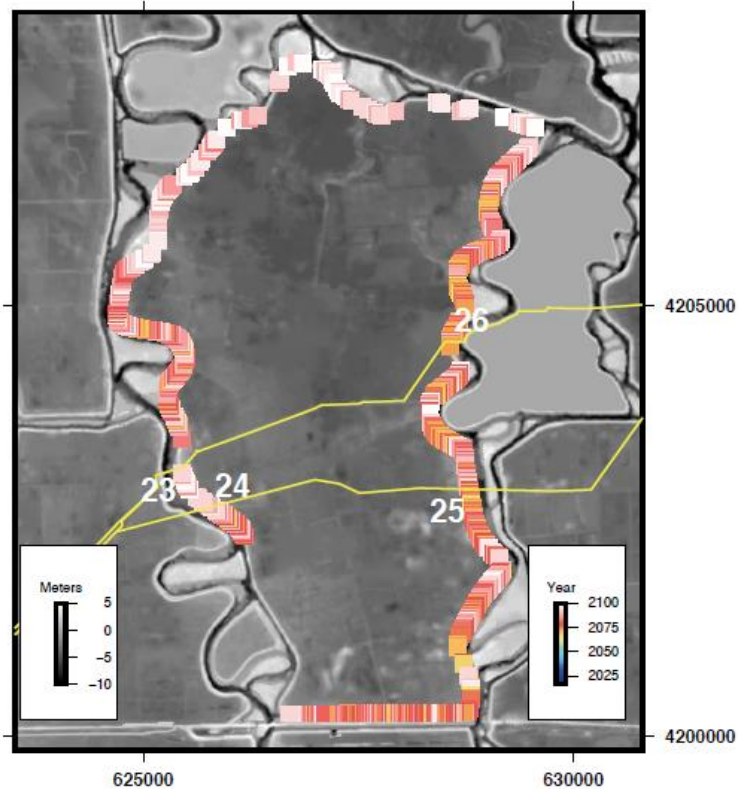
Because of the relative spatial coarseness of the 100-year flood projection (Figure 10) and the SLR projection (Figure 9), the time-to-exceedance gradients are essentially identical to the VLM gradients, in this case, years over distances of 10s of meters (within each scenario, RCP 4.5 or RCP 8.5). For instance, the significantly lower VLM rate on the western side (crossings #23,24) if Bacon Island compared to the eastern side (crossings #26,25) make the western side's exceedance date estimate 25 years later than the eastern side's.

Figure 18a-e. Maps showing exceedance date of the PL84-99 threshold for each of the studied regions for the two SLR end-member case scenarios (RCP 8.5 99% percentile, RCP 4.5 50%). All annotations as in Figure 12. See Figure 1b for locations. All data are second acquisition minus first acquisition, where the first acquisition is the 2007 ALS data set. Second acquisition type indicated in parentheses. A) Bacon Island (MLS). B) Bouldin Island (MLS). C) Isleton/Andrus/Brannon Islands (MLS). D) Jersey Island (MLS). E) Sherman Island (ALS).

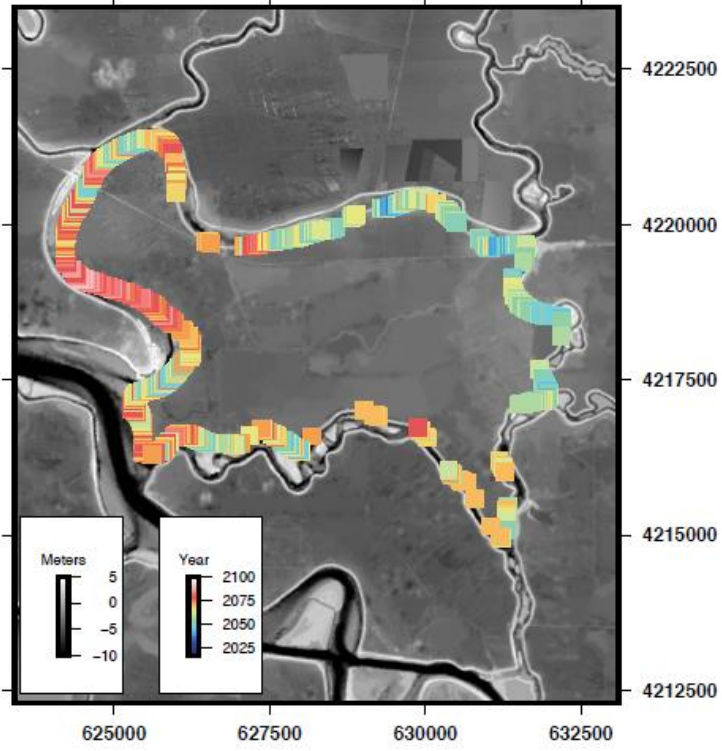
Bacon Island RCP8.5 99%tile



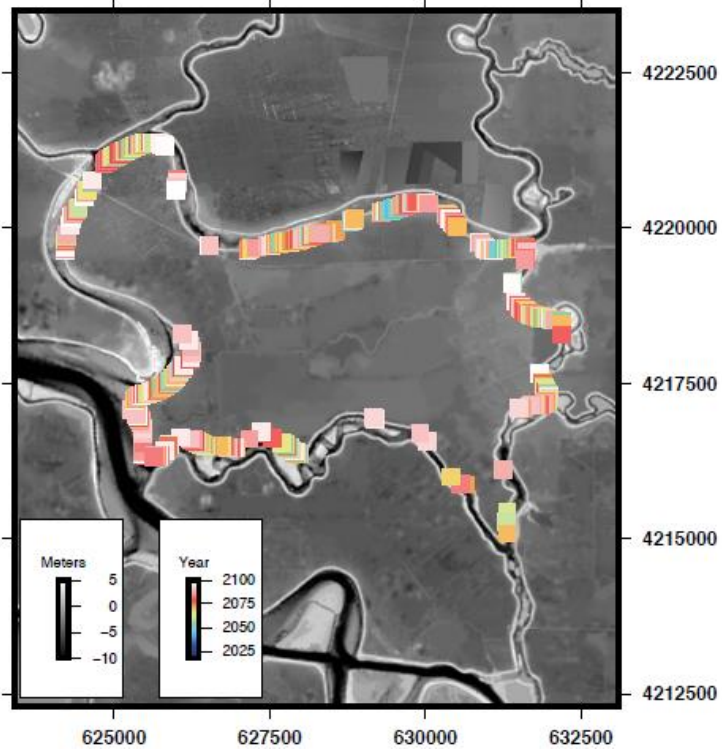
RCP4.5 50%tile



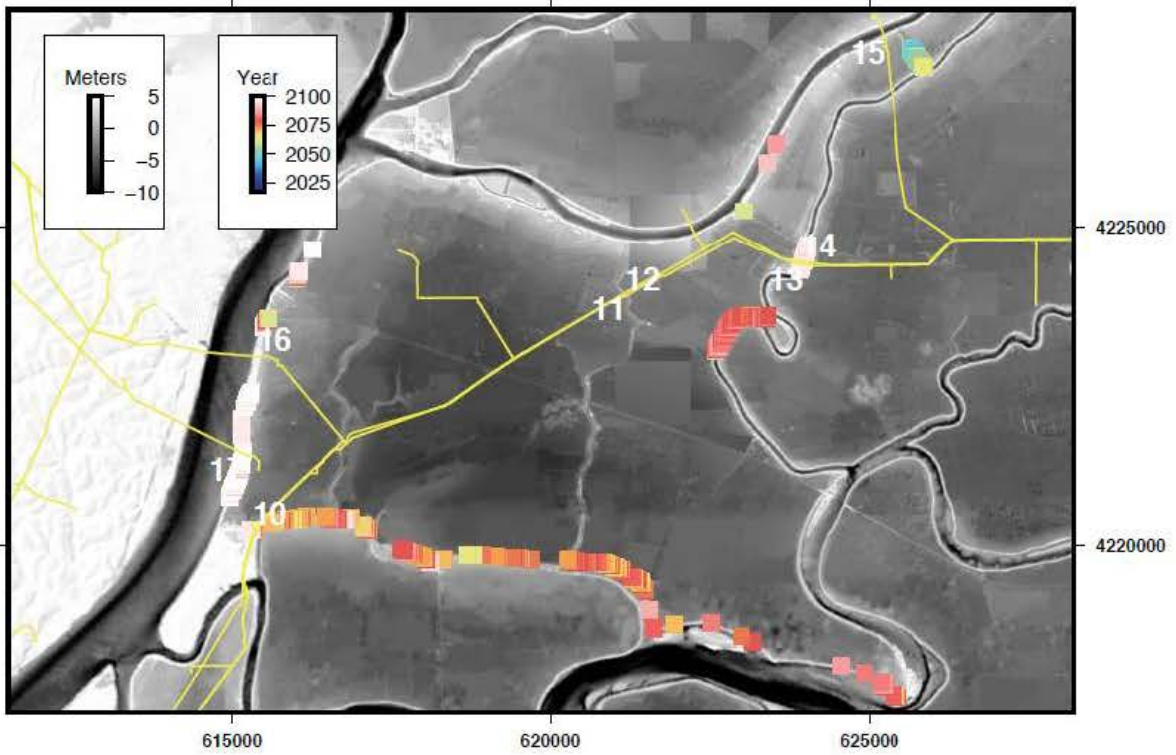
Bouldin Island RCP8.5 99%tile



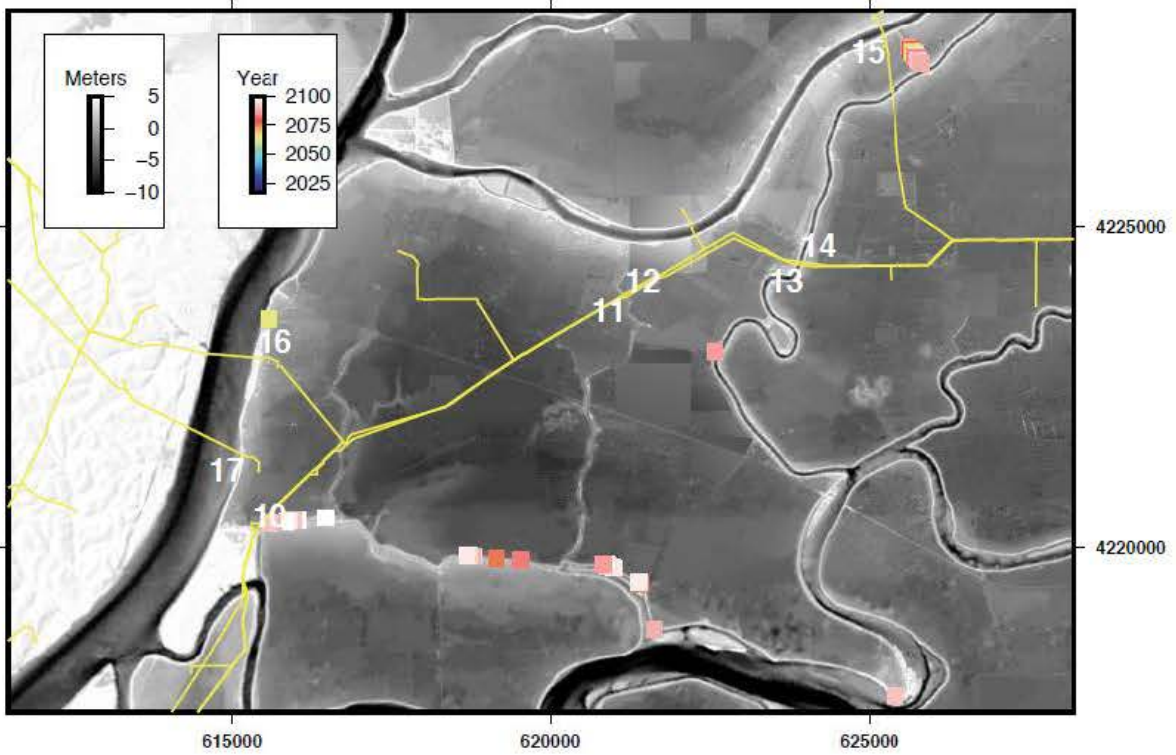
RCP4.5 50%tile



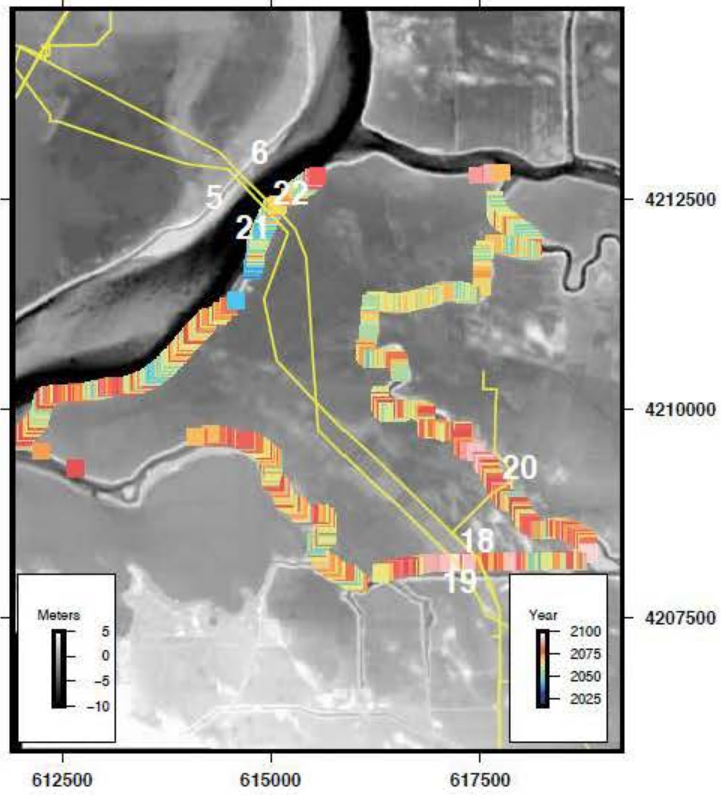
Isleton Region RCP8.5 99%tile



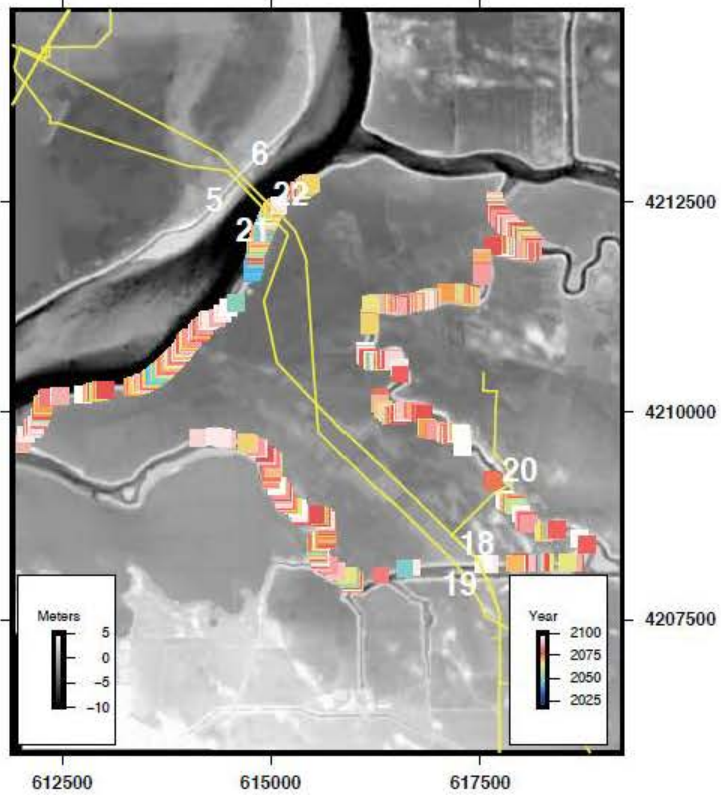
RCP4.5 50%tile



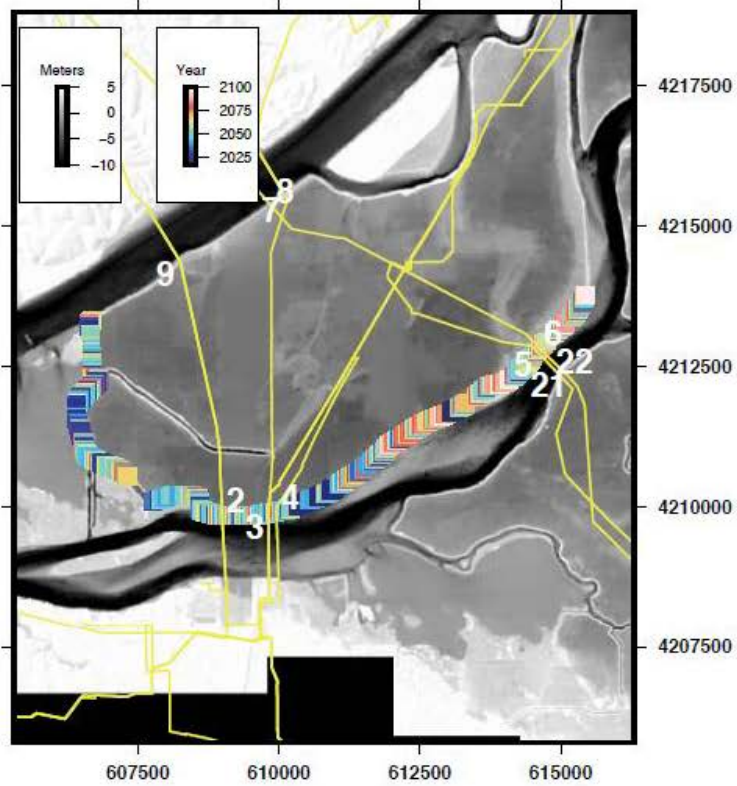
Jersey Island RCP8.5 99%tile



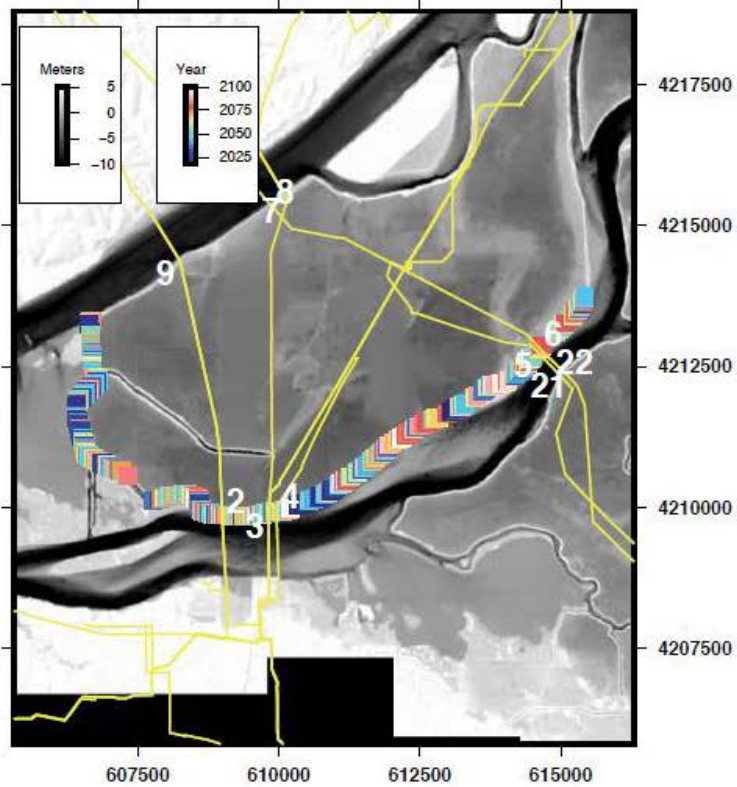
RCP4.5 50%tile



Sherman Island RCP8.5 99%tile



RCP4.5 50%tile



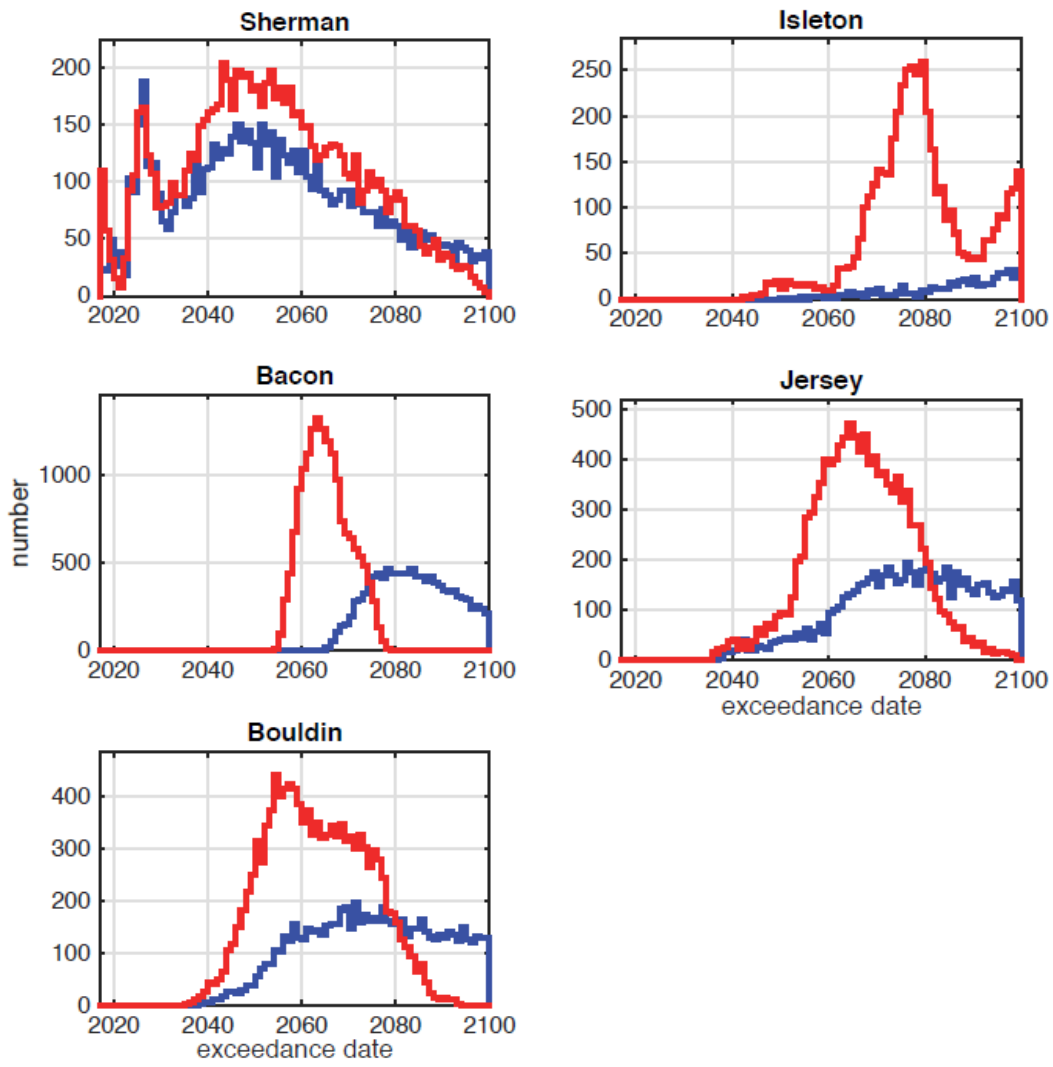


Figure 19. Histogram, for each island region studied, of exceedance date projection for the RCP 8.5 99% (red) and RCP 4.5 50% (blue) scenarios.

3.4 Uncertainty

The 5 terms in equation 1 have varying degrees of uncertainty. The overtopping threshold, $u_{p184-99}$, is exactly defined and has zero uncertainty. Uncertainty in $SLR(t)$ dominates the remaining terms especially when we consider the difference of potential values between the two scenarios (RCP4.5 and 8.5A), presented in Figure 9. For instance, by 2060 the difference in SLR for the two scenarios is greater than 50cm (Figure 9). Accordingly, all of our overtopping projections should be interpreted within the context of the uncertainty represented by the two end-member scenarios presented (Figure 19). Below, for clarity, we discuss some individual uncertainty sources.

Measurement

We evaluated individual LIDAR point error for the three datasets via standard checks with ground-control points. Vertical RMSE (root-mean square error) for the 2007 ALS data is 9.4 cm (https://coast.noaa.gov/htdata/lidar1_z/geoid12a/data/2523/ca2007_cdwr_sanjoaquindelata_metadata.html#4). Vertical RMSE on the 2015 NCALM ALS data is 5 cm and vertical RMSE on the 2015/2016 MLS data is 2 cm (Glennie, Brooks et al. 2013). The RMSE for the ALS – ALS data (Grizzly and Sherman Islands) is 10.6 cm and the RMSE for the ALS – MLS data is 9.6 cm. These RMSE values represent the noise for individual points. Our analysis has much smaller uncertainty, however, because of the averaging and noise reduction that takes place when we grid the data (Section 2.4.4) for the levee analysis. The corresponding error, less than a few centimeters, is indicated graphically by examination of the profiles in Figs. 14 and 15.

Projection

Because the Delta levees are so heavily influenced by anthropogenic activities, there is potential for non-linear consolidation of construction fill material, a well-known phenomenon comprising an initial rapid period of primary consolidation (usually on the order of months to a few years) followed by an asymptotically decaying period of secondary consolidation (Terzaghi 1925). In this case, our assumption of linear subsidence would produce errors of different signs depending on the consolidation stage. A detailed analysis of potential non-linearity of compaction would require knowledge of project dates, fill materials and thicknesses, which are out of the scope of this study. For instance, in the neighboring San Francisco Bay, a recent subsidence study estimated 5-14% potential overestimate by using a linear rate for the asymptotically decaying secondary portions of a compaction time curve (Shirzaei and Bürgmann 2018). For our study, we believe we have largely avoided this issue by eliminating from our analysis the places that were filled during the study period, which are also the places that are most likely to experience primary consolidation (see above, section 3.1).

Seasonal Contamination

We showed previously with GPS and InSAR time-series analysis that, superimposed upon general Delta-wide subsidence, there is an annual sinusoidal VLM variation with a $\sim\pm 1$ cm

amplitude associated with seasonal Sierran snowpack melt and runoff (Brooks, Bawden et al. 2012). Thus, depending on the time of year of LIDAR acquisition compared to the initial acquisition in 2007, there can be a small vertical shift in the entire data set from the seasonal effect. By examining continuous GPS time series from the Delta (e.g. Brooks, Bawden et al., 2012) we find that this could introduce a subsidence rate underestimation of 0.5-1.5 mm/yr in our analysis. This is at least an order of magnitude less than the observed subsidence rates (mms/yr compared to cms/yr) and so we consider it negligible for this study.

4: Discussion

We have shown the utility of using repeat LIDAR surveys (either airborne or truck-mounted) to estimate very precisely and accurately VLM rates on Delta levees. Because LIDAR data generally have very dense acquisition footprints (order of < 1 meter), the VLM maps created by differencing LIDAR data allows for very local analysis over horizontal length-scales of meters to 10s of meters. This permits consideration of subsidence effects both at the scale of, for instance, a Delta island and even at the scale of individual pipeline crossings. The VLM rates that we find are similar to other recent studies in the Delta using different measurement techniques (Deverel and Leighton 2010, Brooks, Bawden et al. 2012, Brooks and Majunath 2012, Sharma, Jones et al. 2016).

VLM estimates created from LIDAR data have the advantage of not being coherence-dependent and so they can record faithfully the large VLM (> 10 cm over 10 years) that has occurred in the Delta. As we describe above, however, mitigation of vegetation signal in the LIDAR data sets is problematic, especially when considering the use of legacy datasets that may be delivered only in some post-processed format. Accordingly, we suggest that the use of LIDAR data for VLM estimates is particularly good for solid targets such as the analysis of levee crowns presented here. Our objective is not to advocate for one method over another; we view all subsidence-measuring methodologies to be complementary for use in the Delta. For instance, the spatial coverage of InSAR is clearly a major strength of the technique, though, as discussed by others (Brooks and Majunath 2012, Sharma, Jones et al. 2016) decorrelation issues are a limiting factor.

When combined with SLR and flood-stage estimates, the creation of a spatially broad, self-consistent VLM data set using the LIDAR methodology permits a probabilistic analysis - at the island and pipeline-crossing scale - of overtopping projections. These maps can then be used directly by parties of interest to inform planning for Delta island levees. When estimating the overtopping potential for the Delta levees, there are 3 spatial scales over which the contributing factors - SLR, flood-stage, and VLM - are most strongly expressed, with SLR the most spatially uniform. Thus, although there are still unknowns about spatial gradients from the San Francisco Bay upstream to the Delta, for a specific stretch of levee, SLR can be considered uniform. Flood-stage estimation is more dependent on the detailed geometry of the river banks and so it can vary more strongly than SLR in the Delta. We refer the reader to the work of Radke et al (2018)

for more detailed flood-stage simulations. As we have shown in this report, VLM can vary strongly over the spatial scales of the levees and so infrastructure overtopping and/or subsidence analyses at those scales must factor in local subsidence gradients.

We recognize that subsidence in Delta environments can have both anthropogenic and natural causes (Meckel, ten Brink et al. 2006, Meckel, Ten Brink et al. 2007, Deverel and Leighton 2010). The objective of this study was not to discriminate between these effects, but rather, to provide rates of VLM most useful in overtopping projections. As we described above, we attempted to avoid the issue of anthropogenic primary compaction (Terzaghi 1925) by using the correlation plots of elevation and VLM rates to identify remediation zones during the time-spans of the data acquisition.

5: Conclusions and Future Directions

The use of LIDAR (either airborne or mobile) is an especially effective technique for assessing vertical land motion associated with the levees in California's Sacramento-San Joaquin Delta, because we can use LIDAR to obtain wider spatial surveys over longer periods, and are able to compensate for the effects of vegetation-caused decorrelation by tracking the subsidence of unvegetated roads. We estimated ~10-year mean subsidence rates of ~1-2 cm/yr for most of the islands we surveyed. We found that the Sherman and Grizzly Island regions have subsidence rates close to a factor of 2 greater than elsewhere. We also found that local subsidence gradients can be on the orders of cms/yr over levee-crest parallel distances of 10s of meters and that these types of gradients are present near some pipeline crossings. Although it is out of the scope of this study to analyze pipeline-specific stresses, it stands to reason that VLM-caused stresses will be concentrated at points along profiles where the change in VLM is greatest. The VLM data could be used to prioritize regions of monitoring if VLM-caused stresses are deemed to be of concern.

For each levee studied, we combine: (1) the estimated subsidence rate, (2) a conservative range of sea-level rise projections and, (3) an estimate of the 100-year flood stage to project the time until exceedance of the federal levee height standard (PL84-99). Our projections indicate general ranges of exceedance date from ~2060 (fast sea-level rise scenario) to 2080 (slow sea-level rise scenario) with some places projected to exceed threshold ~2050.

In the future, these projections can be refined by acquiring repeat LIDAR surveys to assess any non-linearity of rates. Additionally, refined modeling of 100-year flood stage spatial variability will also provide more accurate overtopping projections.

6: References

- Amos, C. B., P. Audet, W. C. Hammond, R. Bürgmann, I. A. Johanson and G. Blewitt (2014). "Uplift and seismicity driven by groundwater depletion in central California." Nature **509**(7501): 483 %@ 1476-4687.
- Bawden, G. W., J. Howle, S. Bond, M. Shriro and P. Buck (2014). "Three-dimensional imaging, change detection, and stability assessment during the centerline trench levee seepage experiment using terrestrial light detection and ranging technology, Twitchell Island, California, 2012." US Geol Surv Open-File Rep 2014-1092.
- Board, O. S. (2012). Sea-Level Rise for the Coasts of California, Oregon, and Washington: Past, Present, and Future, National Academies Press.
- Brooks, B. A., G. Bawden, D. Manjunath, C. Werner, N. Knowles, J. Foster, J. Dudas and D. Cayan (2012). "Contemporaneous Subsidence and Levee Overtopping Vulnerability, Sacramento-San Joaquin Delta, California " San Francisco Estuary and Watershed Science **10**(1).
- Brooks, B. A., C. Glennie, K. W. Hudnut, T. Ericksen and D. Hauser (2013). "Mobile Laser Scanning Applied to the Earth Sciences." Eos **94**(36): 313-315.
- Brooks, B. A. and D. Majunath (2012). Twenty-First Century Levee Overtopping Projections from InSAR-Derived Subsidence Rates in the Sacramento-San Joaquin Delta, California: 2006–2010. California Energy Commission. Publication number: CEC-500-2012-018. C. E. C. P. n. CEC-500-2012-018.
- Brooks, B. A., M. Merrifield, J. Foster, C. Werner, F. B. Gomez, M. and S. Gill (2007). "Space Geodetic Determination of Spatial Variability in Relative Sea Level Change, Los Angeles Basin." Geophysical Research Letters **34**(L01611): doi:10.1029/2006GL028171.
- Cayan, D. R., J. Kalansky, S. Iacobellis and D. Pierce (2016). Creating Probabilistic Sea Level Rise Projections to support the 4th California Climate Assessment, California Energy Commission. **Docket #: 16-IEPR-04**.
- Church, J. A. and N. J. White (2006). "A 20th century acceleration in global sea-level rise." Geophys. Res. Lett. **33**(L01602).
- Coons, T., C. E. Soulard and N. Knowles (2008). "High-Resolution Digital Terrain Models of the Sacramento/San Joaquin Delta Region, California." U.S. Geological Survey Data Series **359**.
- DeConto, R. M. and D. Pollard (2016). "Contribution of Antarctica to past and future sea-level rise." Nature **531**(7596): 591-597.

- Department of the Army, S. D., Corps of Engineers (1976). Sacramento-San Joaquin Delta California: Stage-Frequency Study Hydrology. Sacramento, CA.
- Department of the Army, S. D., Corps of Engineers (1982). Sacramento-San Joaquin Delta California: Documentation Report. Sacramento, CA.
- Department of the Army, S. D., Corps of Engineers (1992). Sacramento-San Joaquin Delta California: Special Study Hydrology. Sacramento, CA.
- Deverel, S. J. and D. A. Leighton (2010). "Historic, Recent, and Future Subsidence, Sacramento-San Joaquin Delta, California, USA." San Francisco Estuary and Watershed Science 8(2): 1-23.
- Deverel, S. J. and S. Rojstaczer (1996). "Subsidence of agricultural lands in the Sacramento-San Joaquin Delta, California: Role of aqueous and gaseous carbon fluxes." Water Resources Research 32(8): 2359-2367.
- Deverel, S. J., B. Wang and S. Rojstaczer (1998). Subsidence of organic soils, Sacramento-San Joaquin Delta. Land subsidence case studies and current research. Proceedings of the Joseph Poland Subsidence Symposium. Sudbury (MA): Association of Engineering Geologists. J. W. Borchers. Belmont, CA, Star Publishing Company: 489-502.
- Dudas, J. (2009). "Delta Lidar." California Surveyor 158.
- Glennie, C., B. A. Brooks, T. Ericksen, D. Hauser, K. Hudnut, J. Foster and J. Avery (2013). "Compact Multipurpose Kinematic LiDAR Scanning System – Initial Tests and Results." Remote Sensing 5(2): 521-538.
- Glennie, C. L., W. E. Carter, R. L. Shrestha and W. E. Dietrich (2013). "Geodetic imaging with airborne LiDAR: the Earth's surface revealed." Reports on progress in physics. Physical Society 76(8): 086801.
- Griggs, G., J. Árvai, D. Cayan, R. DeConto, J. Fox, H. Fricker, R. Kopp, C. Tebaldi, E. Whiteman, (California, O. P. C. Science and A. T. W. Group). (2017). "Rising Seas in California: An Update on Sea-Level Rise Science. ." California Ocean Science Trust.
- Hammond, W. C., G. Blewitt and C. Kreemer (2016). "GPS Imaging of vertical land motion in California and Nevada: Implications for Sierra Nevada uplift." Journal of Geophysical Research: Solid Earth 121(10): 7681-7703 %@ 2169-9356.
- Heberger, M., H. Cooley, P. Herrera, P. H. Gleick and E. Moore (2009). "The impacts of sea-level rise on the California coast." California Climate Change Center CEC-500-2009-024-E.
- Huang, W.-C., M.-C. Weng and R.-K. Chen (2014). "Levee failure mechanisms during the extreme rainfall event: a case study in Southern Taiwan." Natural Hazards 70(2): 1287-1307 %@ 0921-1030X.

- Kennedy, R., S. Bauer, L. Brathwaite, P. Puglia, J. Gonzales and K. Anderson (2014). "2013 Natural Gas Issues, Trends, and Outlook." Final Staff Report (No. CEC-200-2014-001-SF). California Energy Commission..
- Kopp, R. E., R. M. Horton, C. M. Little, J. X. Mitrovica, M. Oppenheimer, D. Rasmussen, B. H. Strauss and C. Tebaldi (2014). "Probabilistic 21st and 22nd century sea - level projections at a global network of tide - gauge sites." Earth's future **2**(8): 383-406.
- Meckel, T. A., U. S. ten Brink and S. J. Williams (2006). "Current subsidence rates due to compaction of Holocene sediments in southern Louisiana." Geophysical Research Letters **33**(11).
- Meckel, T. A., U. S. Ten Brink and S. J. Williams (2007). "Sediment compaction rates and subsidence in deltaic plains: numerical constraints and stratigraphic influences." Basin Research **19**: 19-31.
- Mount, J. and R. Twiss (2005). "Subsidence, sea level rise, seismicity in the Sacramento-San Joaquin Delta." San Francisco Estuary and Watershed Science **3**(1): Article 5.
- Needham, H. F., D. P. Brown and L. M. Carter (2012). Impacts and adaptation options in the Gulf Coast, Center for Climate and Energy Solutions.
- Ojha, C. S. P., V. P. Singh and D. D. Adrian (2001). "Influence of porosity on piping models of levee failure." Journal of geotechnical and geoenvironmental engineering **127**(12): 1071-1074 %@ 1090-0241.
- Pearson, C. and R. Snay (2013). "Introducing HTDP 3.1 to transform coordinates across time and spatial reference frames." GPS solutions **17**(1): 1-15.
- Radke, J. D., G. S. Biging, M. Schmidt-Poolman, H. Foster, E. Roe, Y. Ju, O. Hoes, T. Beach, A. Alruheil, L. Meier, W. Hsu, R. Neuhausler, W. Fourt, W. Lang, U. Garcia and I. Reeves (2016). "Assessment of Bay Area Natural Gas Pipeline Vulnerability to Climate Change." California Energy Commission. Publication number: CEC-500-2017-008.
- Radke, J.D, G.S. Biging, K. Rovers, M. Schmidt-Poolman, H. Foster, E. Roe, Y. Ju, S. Lindbergh, T. Beach, L. Maier, Y. He, M. Ashenfarb, P. Norton, M. Wray, A. Alruheil, S. Yi, R. Rau, J. Collins, D. Radke, M. Coufal, S. Marx, D. Moanga, V. Ulyashin, A. Dalal. (University of California, Berkeley). 2018. ***Assessing Extreme Weather-Related Vulnerability and Identifying Resilience Options for California's Interdependent Transportation Fuel Sector***. California's Fourth Climate Change Assessment, California Energy Commission. Publication Number: CCCA4-CEC-2018-012.
- Rojstaczer, S. and S. J. Deverel (1993). "Time dependence in atmospheric carbon inputs from drainage of organic soils." Geophys. Res. Lett. **20**: 1383-1386.

- Rojstaczer, S. and S. J. Deverel (1995). "Land Subsidence in Drained Histosols and Highly Organic Mineral Soils of California." Soil Sci Soc Am J **59**(4): 1162-1167.
- Rojstaczer, S., R. E. Hamon, S. J. Deverel and C. Massey (1991). "Evaluation of selected data to assess the causes of subsidence in the Sacramento-San Joaquin Delta, California." U.S. Geological Survey, Open-File Report 91-193: 16.
- Serre, D., L. Peyras, R. Tourment and Y. Diab (2008). "Levee performance assessment methods integrated in a GIS to support planning maintenance actions." Journal of Infrastructure Systems **14**(3): 201-213 %@ 1076-0342.
- Sharma, P., C. E. Jones, J. Dudas, G. W. Bawden and S. Deverel (2016). "Monitoring of subsidence with UAVSAR on Sherman Island in California's Sacramento–San Joaquin Delta." Remote Sensing of Environment **181**: 218-236.
- Shirzaei, M. and R. Bürgmann (2018). "Global climate change and local land subsidence exacerbate inundation risk to the San Francisco Bay Area." Science Advances **4**(3).
- Sills, G. L., N. D. Vroman, R. E. Wahl and N. T. Schwanz (2008). "Overview of New Orleans levee failures: lessons learned and their impact on national levee design and assessment." Journal of Geotechnical and Geoenvironmental Engineering **134**(5): 556-565 %@ 1090-0241.
- Suddeth, R. J., J. F. Mount and J. R. Lund (2010). "Levee Decisions and Sustainability for the Sacramento-San Joaquin Delta." San Francisco Estuary and Watershed Science **8**(2): 1-23.
- Terzaghi, K. (1925). "Principles of soil mechanics, IV—Settlement and consolidation of clay." Engineering News-Record **95**(3): 874-878.
- Tung, Y. K. and L. W. Mays (1981). "Risk models for flood levee design." Water Resources Research **17**(4): 833-841 %@ 1944-7973.
- Wang, C. and N. F. Glenn (2009). "Integrating LiDAR intensity and elevation data for terrain characterization in a forested area." IEEE Geoscience and Remote Sensing Letters **6**(3): 463-466.
- Woppelmann, G., C. Letetrel, A. Santamaria, M.-N. Bouin, X. Collilieux, Z. Altamimi, S. D. P. Williams and B. M. Miguez (2009). "Rates of sea-level change over the past century in a geocentric reference frame." Geophys. Res. Lett. **36**(L12607); doi:10.1029/2009GL038720.

APPENDIX A: VLM Rate Plots for Natural Gas Pipeline Crossings

This Appendix features image A1, which comprises twenty-two maps showing Final VLM rate plots for all numbered pipeline crossings. See Figure 16 for locations. For each of the plots, the pipeline crossing location is indicated with the grey box. For ease of reference, the crossing location serves as a local origin and the distances on the horizontal and vertical axes are with respect to this local origin. Crossings 10,13, and 14 are not plotted because of a paucity of data within 50 meters of the crossing location.

